

Conditional HI mass functions and the HI-to-halo mass relation in the local Universe

XIAO LI ¹, CHENG LI ¹, H.J. MO ², TING XIAO ³, AND JING WANG ⁴

¹*Department of Astronomy, Tsinghua University, Beijing 100084, China*

²*Department of Astronomy, University of Massachusetts Amherst, MA 01003, USA*

³*Department of Physics, Zhejiang University, Hangzhou, Zhejiang 310027, China*

⁴*Kaoli Institute for Astronomy and Astrophysics, Peking University, Beijing 100871, China*

ABSTRACT

We present a new HI mass estimator which relates the logarithm of the HI-to-stellar mass ratio to a linear combination of four galaxy properties: stellar surface mass density, color index $u - r$, stellar mass and concentration index, with the scatter of individual galaxies around the mean HI mass modeled with a Gaussian distribution function. We calibrate the estimator using the xGASS sample, including both HI detection and non-detection, and constrain the model parameters through Bayesian inferences. Tests with mock catalogs demonstrate that our estimator provides unbiased HI masses for optical samples like the SDSS, thus suitable for statistical studies of HI gas contents in galaxies and dark matter halos. We apply our estimator to the SDSS spectroscopic sample to estimate the HI mass function (HIMF) of local galaxies, as well as the conditional HI mass function (CHIMF) in galaxy groups and the HI-halo mass (HIHM) relation. Our HIMF agrees with the ALFALFA measurements at $M_{\text{HI}} \gtrsim 5 \times 10^9 M_{\odot}$, but with higher amplitude and a steeper slope at lower masses. We show that this discrepancy is caused primarily by the cosmic variance which is corrected for the SDSS sample but not for the ALFALFA. The CHIMFs for all halo masses can be described by a single Schechter function, and this is true for red, blue and satellite galaxies. For central galaxies the CHIMFs show a double-Gaussian profile, with the two components contributed by the red and blue galaxies, respectively. The total HI mass in a group increases monotonically with halo mass. The HI mass of central galaxies in galaxy groups increases rapidly with halo mass only at $M_{\text{h}} \lesssim 10^{12} M_{\odot}$, while the mass dependence becomes much weaker at higher halo masses. The observed HI-halo mass relation is not reproduced by current hydrodynamic simulations and semi-analytic models of galaxy formation.

Keywords: Neutral hydrogen clouds (690), Galaxy dark matter halos (1880)

1. INTRODUCTION

Galaxies are believed to form at the center of dark matter halos through gas cooling and condensation (White & Rees 1978; Mo et al. 2010). Theoretical studies of the HI-to-halo mass (HIHM) relation based on hydrodynamic simulations or halo-based models in recent years (Hess & Wilcots 2013; Barnes & Haehnelt 2014; Guo et al. 2017; Villaescusa-Navarro et al. 2018; Paul et al. 2018; Obuljen et al. 2019; Davé et al. 2020;

Chauhan et al. 2020, 2021; Calette et al. 2021b; Li et al. 2022) have suggested that the majority of the cold gas in the Universe, mostly in neutral (atomic) hydrogen (HI) and molecular hydrogen (H₂), is expected to be in individual galaxies, with a small amount in the circum-galactic medium (CGM) and intergalactic medium (IGM). On the other hand, both theoretical studies and observations have shown that some of the cold gas may be thrown out of galaxies due to galactic winds driven by stellar and AGN feedback or environmental effects such as tidal stripping and ram-pressure stripping in massive halos. Clearly, measurements of HI gas mass for large samples of galaxies down to small gas fractions and over large sky coverage and redshift ranges

Corresponding author: Xiao Li & Cheng Li
li-x19@mails.tsinghua.edu.cn
cli2015@tsinghua.edu.cn

are needed to provide stringent constraints on models of galaxy formation.

Large surveys of HI 21cm emission of galaxies have become available only in the past two decades, such as the HI Parkes All-Sky Survey (HIPASS; Meyer et al. 2004; Wong et al. 2006) and the Arecibo Legacy Fast ALFA (ALFALFA; Giovanelli et al. 2005). High spatial resolution surveys with interferometers are also becoming available, such as the APERTure Tile In Focus array imaging survey (Apertif; Adams et al. 2022). These surveys have detected HI emission from tens of thousands of galaxies up to $z \sim 0.06$, covering large areas in the sky. As expected, most (if not all) cases of the HI detection are associated with optically-identified galaxies in the same sky position and redshift (Haynes et al. 2018). Both HIPASS and ALFALFA have yielded measurements of the HI mass function (HIMF) for the local galaxy population over a mass range nearly five orders of magnitudes from $M_{\text{HI}} \sim 10^6 M_{\odot}$ to $M_{\text{HI}} \sim 10^{11} M_{\odot}$ (Zwaan et al. 2005; Jones et al. 2018a). The two measurements are quite similar to each other, though still with significant differences according to statistical errors, which might be caused by cosmic variance (Jones et al. 2018b; Stevens et al. 2019). Compared to optical surveys, however, current HI surveys are still shallow and biased to gas-rich galaxies. There have been recent efforts to measure the total HI mass in dark matter halos, e.g. by stacking ALFALFA data-cubes of galaxy groups of different halo mass (Guo et al. 2020) or through deep observations of HI emission of individual galaxies (Rhee et al. in preparation). Guo et al. (2020) found a positive correlation between the total HI mass and the dark matter halo mass, with a significant excess of HI mass at $M_h \sim 10^{12} M_{\odot}$, while Rhee et al. (in preparation) observed a nearly flat relation. Chauhan et al. (2021) analyzed possible reasons for the discrepancy between these two studies, and showed that these measurements may not be able to obtain the intrinsic HI-halo mass relation correctly, owing to uncertainties in the halo mass estimate and limitations of the stacking method.

HI samples with depths and sizes comparable to optical surveys, such as the Sloan Digital Sky Survey (SDSS; York et al. 2000), are difficult to obtain in general. As an alternative way to proceed, attempts have been made to estimate HI masses for optically-selected galaxies using their spectral and/or photometric properties, based on the many observational evidences that the galaxy HI mass correlates with optical properties such as stellar mass (Brown et al. 2015), morphology (Haynes & Giovanelli 1984; Toribio et al. 2011; Calette et al. 2021a) and optical size (Haynes & Giovanelli 1984; Jones et al.

2018b). Tremonti et al. (2004) estimated surface gas mass densities for SDSS galaxies from surface densities of star formation rate (given by H α luminosities) by inverting the Kennicutt-Schmidt law (Schmidt 1963; Kennicutt 1998). Meanwhile, Kannappan (2004) found that the HI-to-stellar mass ratio ($\log(M_{\text{HI}}/M_*)$) of local galaxies is linearly correlated with optical (e.g. $u-r$) and optical-to-near IR (e.g. $u-K$) colors, with a scatter of ~ 0.4 dex. Motivated by these studies, Zhang et al. (2009) proposed an estimator for $\log(M_{\text{HI}}/M_*)$ based on a linear combination of the $g-r$ color and i -band surface brightness μ_i , with a scatter of ~ 0.3 dex. They applied the estimator to the SDSS galaxy sample to investigate the variation of HI gas mass fraction on the stellar mass-metallicity relation. A follow-up study by the team of the GALEX Arecibo SDSS Survey (GASS; Catinella et al. 2010) calibrated a similar estimator to link $\log(M_{\text{HI}}/M_*)$ with $NUV-r$ and surface stellar mass density μ_* , which also has a scatter of ~ 0.3 dex. Li et al. (2012, hereafter L12) found that the two-parameter estimators from Zhang et al. (2009) and Catinella et al. (2010) significantly underestimate the HI mass for the ALFALFA sample, which is expected to be biased to HI-rich galaxies. They proposed a new estimator with four galaxy properties: surface stellar mass density μ_* , $NUV-r$, stellar mass M_* and $g-i$ color gradient Δ_{g-i} . With a smaller scatter of ~ 0.2 dex, this estimator was applied to the SDSS sample to study both the HI mass-dependence of the galaxy clustering (L12) and environmental effects on the gas depletion in clusters of galaxies (Zhang et al. 2013).

Using the RESolved Spectroscopy of a Local VolumE survey (RESOLVE; Kannappan et al. in prep.), Eckert et al. (2015) calibrated a relation between the HI gas fraction, color index and axis ratio of galaxies. More recently, Zu (2020, hereafter Z20) developed a two-parameter HI mass estimator by linearly combining stellar mass M_* and $(g-r)$, and used it to study the mass-metallicity relation of SDSS galaxies. To avoid the Malmquist bias produced by limited detection depths of current HI surveys, Z20 designed a likelihood model to account for the detection probability of ALFALFA and constrained the model parameters using Bayesian inferences. Lu et al. (2020) also used a linear combination of M_* and $(g-r)$ to estimate the HI mass of SDSS galaxies, in an attempt to estimate the HI gas content in dark matter halos. In addition to these linear estimators, a few nonlinear models have also been obtained to estimate HI masses of local galaxies, taking advantage of the technique of machine learning (e.g. Teimoorinia et al. 2017; Rafieferantsoa et al. 2018).

In this paper we extend previous studies by developing a new estimator to predict the HI gas content of galaxies in a large optical sample. Our estimator makes improvements in the following aspects. First, we calibrate our HI mass estimator using the xGASS sample (Catinella et al. 2018), and we include galaxies both with and without HI detection in the calibration to reduce bias. Recent studies have mostly used the ALFALFA sample, which is shallow and biased to HI-rich galaxies. Galaxies without HI detection contain useful information about gas-poor galaxies, and so should not be ignored in the calibration in order to obtain an unbiased estimator. Second, we follow L12 to use a linear model using four galaxy properties for the estimator, but we also take into account scatter in the model. This scatter includes not only the intrinsic variance of individual galaxies but also uncertainties in the measurements of the HI mass and optical parameters. Finally, we follow Z20 to constrain model parameters of our estimator using the Bayesian framework, which allows us to explore the model parameter space efficiently, and to better understand the correlations among model parameters. We use mock catalogs to mimic the selection effects of the ALFALFA and xGASS samples and to demonstrate that our estimator is unbiased for SDSS-like samples. We thus can use our estimator to estimate the HIMF of local galaxies, the conditional HIMF and the total HI mass as a function of dark matter halo mass.

We organize our paper as follows. In section 2 we describe the HI and optical samples used in our analysis. In section 3 we present our HI estimator and describe the calibration procedure and test results. In section 4 we apply our HI estimator to the SDSS sample to estimate HI contents of galaxies and their host halos. We discuss and summarize our results in section 5 and section 6. Throughout this paper we assume a flat Λ CDM cosmology with $H_0 = 100h$ km s⁻¹Mpc⁻¹, $h = 0.7$, $\Omega_m = 0.3$, and $\Omega_\Lambda = 0.7$.

2. DATA

2.1. The xGASS sample

We use the xGASS sample to calibrate our HI mass estimator. The xGASS is an extension of the GASS survey, an HI 21cm survey observed with the Arecibo telescope for a sample of galaxies with redshift $0.025 < z < 0.05$ and a flat stellar mass distribution in the range $10^{10}M_\odot < M_* < 10^{11.5}M_\odot$. The sample galaxies are randomly selected from a parent sample of $\sim 12,000$ galaxies located in the overlapping region among SDSS data release six (DR6; Adelman-McCarthy et al. 2008), Galaxy Evolution Explorer (GALEX; Martin et al. 2005) Medium Imaging Survey, and the AL-

FALFA survey footprint. Each galaxy is observed with Arecibo until a significant HI emission line is detected, or the HI to stellar mass ratio reaches an upper limit of $M_{\text{HI}}/M_* \sim 1.5\%$ (see C10 for details). The xGASS extends the survey down to a lower mass limit of 10^9M_\odot , by further observing a sample of galaxies with $9.0 < \log(M_{\text{HI}}/M_\odot) < 10.2$ and¹ $0.01 < z < 0.02$. Here we use the combined xGASS sample constructed by Catinella et al. (2018), which includes 1179 galaxies obtained by GASS and xGASS and supplemented with HI-rich galaxies selected from the ALFALFA $\alpha.70$ sample that are not included in GASS/xGASS.

From the combined xGASS sample we select a subset of galaxies with good measurements. A galaxy is included in our sample if all the following requirements are met: (i) `HIconf_flag` ≤ 0 , (ii) `HI_flag` ≤ 1 , and (iii) $\sigma_{u-r} < 0.3$. Here `HIconf_flag` is the confusion flag provided in the combined xGASS catalog, with `HIconf_flag` = 1 for certain confusion, > 0 for a small companion, 0 for no confusion and -99 for non-detection. Thus, the first criterion selects both detections with no confusion and non-detections from the xGASS sample. The `HI_flag` is the quality flag for xGASS detections, with `HI_flag` ≤ 1 for good quality, 2 for marginal, 5 for confused and 3 for both marginal and confused observations. The error of $u - r$ color, σ_{u-r} , is calculated through error propagation based on the inverse variance of the $u-$ and $r-$ band absolute magnitudes provided in the NASA Sloan Atlas (NSA; Blanton et al. 2011). These restrictions yield a final sample, which contains 625 galaxies each with an HI mass measurement, and 358 galaxies each with only an HI mass upper limit. For those with an HI gas mass measurement, M_{HI} is self-absorption corrected using $\Delta \log M_{\text{HI}} = (0.13 \pm 0.03) \log(a/b)$ (Jones et al. 2018a), where a/b is the major-to-minor axis ratio. We refer to this sample as `SampleX` in the rest of this paper.

2.2. The ALFALFA galaxy sample

The Arecibo Legacy Fast Arecibo L-band Feed Array Survey (ALFALFA; Giovanelli et al. 2005) is a blind survey of HI 21 cm emission over ~ 7000 deg² of the sky and up to redshift $z \sim 0.06$. The final data release, the ALFALFA $\alpha.100$ catalog (Haynes et al. 2018), consists of $\sim 31,500$ extragalactic HI line sources. Two sky areas are covered by ALFALFA: one in the northern Galactic hemisphere and one in the southern Galactic hemisphere. Since our optical sample (see below) is mainly in the northern Galactic hemisphere, we select

¹ For simplicity, we'll denote \log_{10} as \log throughout this paper

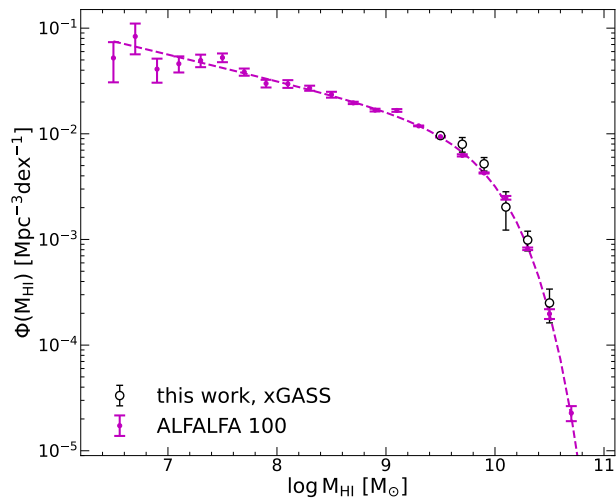


Figure 1. The HIMF of ALFALFA and xGASS survey. The magenta points with errorbar are the ALFALFA 100 percent HIMF datapoints (Jones et al. 2018a). The magenta dashed line is the best fit to the data. The black open circle with errorbar is the xGASS HIMF derived in this work (see subsection 2.3).

from ALFALFA $\alpha.100$ a subsample that covers the sky of $138^\circ < \alpha < 232^\circ$, $0^\circ < \delta < 36.5^\circ$ and the redshift of $0.00 < z < 0.05$. The upper limit in z is set to avoid the contamination of RFI (Haynes et al. 2018). We use ALFALFA sources flagged with Code 1, i.e those with $\text{SNR} \gtrsim 6.5$, together with those flagged with Code 2, i.e. those with $\text{SNR} (\lesssim 6.5)$ but matched with optical counterparts that have redshift consistent with the observed 21cm line. Our ALFALFA galaxy sample consists of 16,400 galaxies. In what follows this sample is referred to as **SampleA**.

2.3. The observed HI mass function

A blind HI survey, such as the ALFALFA, aims to detect all sources above some detection limit, e.g. in 21cm flux. Such a survey is expected to be biased against galaxies with low HI mass. Thus, unlike an HI survey which starts from a given optical sample, such as xGASS described above, a blind survey does not provide a fair sample to study the relationship between HI and optical properties of galaxies. However, being selected on the basis of 21cm flux, blind surveys can provide complete samples to obtain summary statistics, such as the HI mass function (HIMF), above certain HI mass. Such statistics are not direct measurements of the relationship between HI and optical properties, they nevertheless provide constraints on the relationship. In our analysis, we will use the HIMF obtained from ALFALFA as an additional constraint on our model.

As a check of consistency between xGASS and ALFALFA, we show in Figure 1 the HIMFs obtained from these two samples. The ALFALFA measurements are adopted from Jones et al. (2018a) and shown as the magenta error bars, together with the fitting to a Schechter function shown by the magenta dashed line. The HIMF for xGASS is estimated by us using the xGASS representative sample (**SampleX**). To that end, we assign a weight $w_{i1}w_{i2}$ to the i -th galaxy in **SampleX**, where w_{i1} accounts for the mass-dependent selection of **SampleX** with respect to the SDSS galaxy sample (**SampleS**), and w_{i2} corrects for the selection effect of **SampleS** using the $1/V_{\text{max}}$ weighting scheme (see subsection 4.1 for more details). We only obtain the xGASS HIMF at $\log M_{\text{HI}}/M_\odot > 9.5$ to avoid influences of non-detection and incompleteness at the low-mass end. The errors of the HIMF are estimated by bootstrap resampling of the galaxies in **SampleX**. As one can see from the figure, at $\log M_{\text{HI}}/M_\odot > 9.5$, both the xGASS and ALFALFA measurements are consistent with each other. To ensure consistency, we only use the ALFALFA measurements of the HIMF at $\log M_{\text{HI}}/M_\odot > 9.5$ as additional constraints on our HI estimator.

2.4. The SDSS galaxy sample

We select our optical galaxy sample from the New York University Value Added Galaxy Catalog (NYU-VAGC)² constructed by Blanton et al. (2005) from the SDSS spectroscopic galaxy sample. We start with the VAGC post-redshift sample **bbright0**, which contains 535,192 galaxies with spectroscopically measured redshifts and brighter than $r = 17.6$ mag, where r is the r -band apparent Petrosian magnitude corrected for Galactic extinction. We restrict ourselves to the redshift range of $0.003 < z < 0.05$, where the upper redshift limit is set to match the HI galaxy sample and the lower limit is set to avoid large uncertainties in distances produced by peculiar motions of nearby galaxies. This gives us a sample of 86,487 galaxies. We refer to this sample as **SampleS** in the rest of this paper. We will apply our HI mass estimator to this sample and derive the statistical properties of HI gas contents for both galaxies and their host dark matter halos (see section 4).

2.5. The NSA and galaxy properties

To design our HI mass estimator, we obtain, for each galaxy in the xGASS, ALFALFA and SDSS samples described above, the following set of properties from the NSA³:

² <http://sdss.physics.nyu.edu/vagc/>

³ <http://www.nsatlas.org/>

- M_* : stellar mass in units of solar mass, estimated with `kcorrect v4.2`,⁴ (Blanton & Roweis 2007) which performs SED fitting to the SDSS photometric data based on the stellar spectral templates from Bruzual & Charlot (2003) using the stellar initial mass function of Chabrier (2003) and the Padova 1994 isochrones, and the ionized gas emission spectral templates of Kewley et al. (2001).
- μ_* : the surface stellar mass density, defined as $M_*/(2\pi R_{50}^2)$, where R_{50} , in units of kpc, is the radius enclosing a half of the total light in r -band.
- $u - r$: the $u - r$ color index, given by the K-corrected absolute magnitude difference between u - and r -band using elliptical Petrosian photometry of SDSS images.
- $NUV - r$: the $NUV - r$ color index, where NUV is the K-corrected magnitude in the NUV -band using elliptical Petrosian photometry of GALEX images.
- R_{90}/R_{50} : the concentration index defined as the ratio between R_{90} (the radius enclosing 90% of the total light in r -band) and R_{50} .

About 5% of the galaxies in **SampleS** do not have counterparts in the NSA. We have examined the effects of these missing galaxies on our results and found that they are negligible. Figure 2 displays the distribution of the **SampleX**, **SampleA** and **SampleS** in the plane of $NUV - r$ color and stellar mass. Galaxies with HI detection and non-detection in **SampleX** are plotted as blue dots and red crosses respectively, respectively. The cyan contours represent the distribution of **SampleA**. The grey 2D histogram and dots indicate **SampleS**. We can see that **SampleA** galaxies are mainly located in the star-forming sequence with $NUV - r \lesssim 4$. Compared to **SampleA**, **SampleX** covers a larger region in parameter space (although it is limited to $M_* > 10^9 M_\odot$ and with a smaller sample size), thus can better represent the general galaxy population. Therefore, we use **SampleX** to calibrate our HI mass estimator.

3. PREDICTING THE HI MASS OF GALAXIES

3.1. The HI mass estimator

Consider a sample of N_g galaxies indexed by i , each of which has a set of observational parameters, \mathbf{x}_i , in addition to the HI observation, y_i . We aim to calibrate a general relation between y and \mathbf{x} so that it can be

⁴ <http://kcorrect.org>

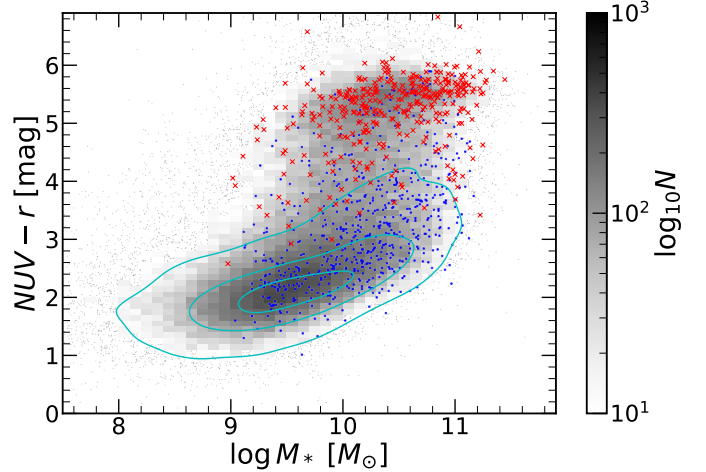


Figure 2. The distribution of our galaxy samples in $NUV - r$ color and stellar mass diagram. Blue points are HI-detected galaxies in **SampleX** and red crosses indicate HI non-detections in **SampleX**. Cyan contours indicate the distribution of **SampleA** galaxies. From inside to outside, the contours include 16%, 50% and 84% of the **SampleA** respectively. The grey 2D histogram and dots show the distribution of **SampleS** galaxies.

used to reliably predict y from \mathbf{x} for galaxies in other samples. We model this relation as

$$y(\mathbf{x}) = y_0(\mathbf{x}) + \delta y(\sigma), \quad (1)$$

where y_0 gives the mean value of y for galaxies of given \mathbf{x} , and δy quantifies the scatter of individual galaxies around the mean. δy is assumed to be a random variable that follows a Gaussian distribution function with a zero mean and a dispersion of σ . We model the mean of y as a linear combination of \mathbf{x} :

$$y_0(\mathbf{x}) = \boldsymbol{\beta}^T \mathbf{x} + q, \quad (2)$$

where $\boldsymbol{\beta}$ is a vector of model parameters that has the same number of elements as \mathbf{x} , T denotes transpose, and q is a constant. In this work we choose y to be the HI-to-stellar mass ratio in logarithmic scale, $y = \log(M_{\text{HI}}/M_*)$, and We use **SampleX** to calibrate model parameters. For \mathbf{x} , we adopt the following four parameters: the surface stellar mass density μ_* , the color index $u - r$, the stellar mass M_* and the concentration index R_{90}/R_{50} (see § 2.5). Thus

$$y = \log \frac{M_{\text{HI}}}{M_*}, \quad \mathbf{x} = \begin{pmatrix} \log \mu_* \\ u - r \\ \log M_* \\ \log \frac{R_{90}}{R_{50}} \end{pmatrix}, \quad \boldsymbol{\beta} = \begin{pmatrix} a \\ b \\ c \\ d \end{pmatrix}. \quad (3)$$

It is not straightforward to design an appropriate functional form for σ . Our tests showed that the scatter

actually depends on $m_0 \equiv y_0 + \log M_*$, that is, the logarithm of the mean value of HI-to-stellar mass ratio, as given by the HI estimator, plus the logarithm of the stellar mass. The dependence can be described by a piecewise linear function:

$$\sigma(m_0) = \begin{cases} |c_a m_0 + c_b|, & \text{if } m_0 \geq m_{0,t} \\ |c_a m_{0,t} + c_b|, & \text{if } m_0 < m_{0,t} \end{cases} \quad (4)$$

where c_a and c_b are model parameters to be determined, and $m_{0,t}$ is an empirically determined cut in m_0 below which the scatter is a constant. Our model thus has a total of 7 free parameters: a, b, c, d, q, c_a, c_b , to be determined. The four-parameter model for the mean relation (Equation 2) is motivated by that in L12 where the HI-to-stellar mass ratio of galaxies was considered as a function of μ_* , $NUV - r$, M_* and the radial gradient of $g - i$. Here we replace the $g - i$ color gradient by the concentration index which is more widely used and easier to measure. We also replace $NUV - r$ by $u - r$ for similar reasons. We note that our model and that of L12 lead to similar results in terms of estimating the mean relation between HI gas mass and galaxy properties. We have attempted to include more parameters or to replace some of the parameters, and found no significant improvements. As pointed out in the introduction, our HI mass estimator is an improvement on earlier estimators because of the inclusion of both the scatter in the model and non-detections in the calibration sample.

3.2. Bayesian inferences of model parameters

We make Bayesian inferences for the model parameters of our HI mass estimator. In what follows we denote the set of model parameters as $\boldsymbol{\theta} \equiv \{a, b, c, d, q, c_a, c_b\}$. We use a combination of two sets of observational data. The first set includes measurements of the four galaxy properties and the HI-to-stellar mass ratio for all individual galaxies in **SampleX**, and is denoted as $\mathbf{D} \equiv \{\mathbf{x}_i, y_i\}$ ($i = 1, \dots, N_g$), where N_g is the number of galaxies in the sample. The second set is the HIMF estimated from ALFALFA, and is denoted as $\Phi_{\text{HI}} \equiv \Phi(M_{\text{HI}}) = \{\Phi_{\text{HI},j}\}$ ($j = 1, \dots, N_m$), with N_m the number of mass bins of the HIMF. Applying Bayes Theorem, we can write the likelihood of $\boldsymbol{\theta}$ given both \mathbf{D} and Φ_{HI} as

$$\begin{aligned} P(\boldsymbol{\theta}|\Phi_{\text{HI}}, \mathbf{D}) &= \frac{P(\Phi_{\text{HI}}, \mathbf{D}|\boldsymbol{\theta}) \cdot P(\boldsymbol{\theta})}{P(\Phi_{\text{HI}}, \mathbf{D})} \\ &= \frac{P(\Phi_{\text{HI}}|\boldsymbol{\theta}) \cdot P(\mathbf{D}|\boldsymbol{\theta}) \cdot P(\boldsymbol{\theta})}{P(\Phi_{\text{HI}}) \cdot P(\mathbf{D})} \quad (5) \\ &= \frac{P(\Phi_{\text{HI}}|\boldsymbol{\theta}) \cdot P(\boldsymbol{\theta}|\mathbf{D})}{P(\Phi_{\text{HI}})}, \end{aligned}$$

where in the second line we have assumed that the measurements of \mathbf{D} and Φ_{HI} are independent. The third line follows from the Bayes relation,

$$P(\boldsymbol{\theta}|\mathbf{D}) = \frac{P(\mathbf{D}|\boldsymbol{\theta}) \cdot P(\boldsymbol{\theta})}{P(\mathbf{D})} \quad (6)$$

where $P(\boldsymbol{\theta}|\mathbf{D})$ is the posterior distribution of $\boldsymbol{\theta}$ inferred from \mathbf{D} alone. The above equations show that we can derive $P(\boldsymbol{\theta}|\Phi_{\text{HI}}, \mathbf{D})$ in two steps. First, we obtain $P(\boldsymbol{\theta}|\mathbf{D})$ from \mathbf{D} using an assumed prior distribution $P(\boldsymbol{\theta})$. Second, we infer $P(\boldsymbol{\theta}|\Phi_{\text{HI}}, \mathbf{D})$ from Φ_{HI} using $P(\boldsymbol{\theta}|\mathbf{D})$ as the prior.

We start by deriving $P(\boldsymbol{\theta}|\mathbf{D})$ using Equation 6. Assuming that galaxies are sampled with an inhomogeneous Poisson process, we can write Equation 6 in logarithmic form as

$$\begin{aligned} \ln P(\boldsymbol{\theta}|\mathbf{D}) &= \ln P(\mathbf{D}|\boldsymbol{\theta}) + \ln P(\boldsymbol{\theta}) - \ln P(\mathbf{D}) \\ &= \sum_{i \in S_d} \ln P_{d,i}(y_i|\boldsymbol{\theta}, \mathbf{x}_i) + \sum_{i \in S_n} \ln P_{n,i}(y_i|\boldsymbol{\theta}, \mathbf{x}_i) \\ &\quad + \text{const.} \end{aligned} \quad (7)$$

Here we have assumed a flat prior distribution for all model parameters, so that $\ln P(\boldsymbol{\theta})$ and the data distribution $P(\mathbf{D})$ both become constant and can be ignored. In the second equation S_d and S_n denote the subsets of galaxies in **SampleX** with and without HI detection, respectively, while $P_{d,i}$ and $P_{n,i}$ are the corresponding likelihoods of y_i given $\boldsymbol{\theta}$ and \mathbf{x}_i . The likelihood for the i -th galaxy to have an HI detection is modeled by

$$P_{d,i}(y_i|\boldsymbol{\theta}, \mathbf{x}_i) = \frac{1}{\sqrt{2\pi}\sigma_i} \exp\left\{-\frac{(y_i - y_{0,i})^2}{2\sigma_i^2}\right\}, \quad (8)$$

where $y_{0,i} = y_{0,i}(\mathbf{x}_i)$ is the mean value predicted by Equation 2, and $\sigma_i = \sigma_i(m_{0,i})$ is the scatter given by Equation 4. When calculating σ_i , we set the value of $m_{0,t}$ in Equation 4 to be $m_{0,t} = 8.5$ based on tests which show that our results are insensitive to the exact value of $m_{0,t}$. We note that, for simplicity, we have neglected the measurement error of \mathbf{x} in Equation 8, which we find to cause a difference of only ~ 0.01 dex in the predicted HI mass of our galaxies and thus have little effect on our results. For non-detections with only upper limits of y_i , we assume they follow the same conditional distribution as detections, so that the likelihood $P_{n,i}$ can be calculated by integrating $P_{d,i}$ over $y \leq y_i$, i.e.

$$P_{n,i}(y_i|\boldsymbol{\theta}, \mathbf{x}_i) = \int_{-\infty}^{y_i} P_{d,i}(y'|\mathbf{x}_i, \boldsymbol{\theta}) dy'. \quad (9)$$

We use the Python package **emcee** to perform Markov chain Monte Carlo (MCMC) sampling over the parameter space (Foreman-Mackey et al. 2013), and obtain

the posterior distribution of the model parameters using Equation 7. During this process we weight each galaxy in **SampleX** in such a way that the stellar mass distribution estimated by the weighted galaxies matches the stellar mass function (GSMF) in the local universe as measured by Chen et al. (2019) (see their Table 1). The posterior distributions of all the model parameters obtained this way are plotted in Figure 3 as blue contours.

Next, we use the ALFALFA HIMF $\Phi(M_{\text{HI}})$ at $\log M_{\text{HI}}/M_{\odot} > 9.5$ to further constrain our model parameters, adopting the likelihood derived above, $P(\theta|\mathbf{D})$, as the prior. Again, we write the last equation in Equation 5 in logarithmic form as

$$\begin{aligned} \ln P(\theta|\Phi_{\text{HI}}, \mathbf{D}) &= \ln P(\Phi_{\text{HI}}|\theta) + \ln P(\theta|\mathbf{D}) + \text{const.} \\ &= \sum_j \ln P_j(\Phi_{\text{HI},j}|\theta) + \ln P(\theta|\mathbf{D}) + \text{const.}, \end{aligned} \quad (10)$$

where $\Phi_{\text{HI},j}$ is the HIMF measurement in the j -th mass bin, and $P_j(\Phi_{\text{HI},j}|\theta)$ is the likelihood of $\Phi_{\text{HI},j}$ given θ :

$$P_j(\Phi_{\text{HI},j}|\theta) = \frac{1}{\sqrt{2\pi}\Delta_j} \exp \left\{ -\frac{[\Phi_{\text{HI},j} - \Phi'_{\text{HI},j}(\theta)]^2}{2\Delta_j^2} \right\} \quad (11)$$

Here $\Phi'_{\text{HI},j}(\theta)$ is the predicted HIMF in the j -th mass bin derived by applying our HI estimator to **SampleS** using the $1/V_{\text{max}}$ weighting scheme (see subsection 4.1 for more details), and Δ_j is the error of $\Phi_{\text{HI},j}$.

The same MCMC sampling as used in the first step is applied here to derive $P(\theta|\Phi_{\text{HI}}, \mathbf{D})$ in Equation 10. The results are plotted in Figure 3 as red contours. To guarantee convergence we have checked the autocorrelation time τ and we find $N/\tau > 80$ (where N is the length of Markov chains) for all parameters, indicating that the Markov chains have well converged. As expected, $P(\theta|\mathbf{D})$ and $P(\theta|\Phi_{\text{HI}}, \mathbf{D})$ are consistent with each other and the latter are better constrained thanks to the additional information provided by the HIMF. In particular, the posterior distributions of c and e are narrowed significantly. We adopt as our best model with maximum posterior probability: $a = -0.42 \pm 0.20$, $b = -0.82 \pm 0.19$, $c = 0.15 \pm 0.11$, $d = -2.57 \pm 1.30$, $q = 3.57 \pm 0.95$, $c_a = 0.10 \pm 0.08$ and $c_b = -1.20 \pm 0.76$. The average HI-to-stellar mass ratio of galaxies at fixed stellar mass is predicted to have negative correlations with μ_* , $u-r$ and R_{90}/R_{50} , which is consistent with direct observations (e.g. Kannappan 2004; Zhang et al. 2009; Catinella et al. 2010). There is some degeneracy among model parameters. For instance, q shows negative correlations with a and a positive correlation with b . We note that c_a and c_b are strongly degenerated, possibly due to the strong constraint to the scatter from the data.

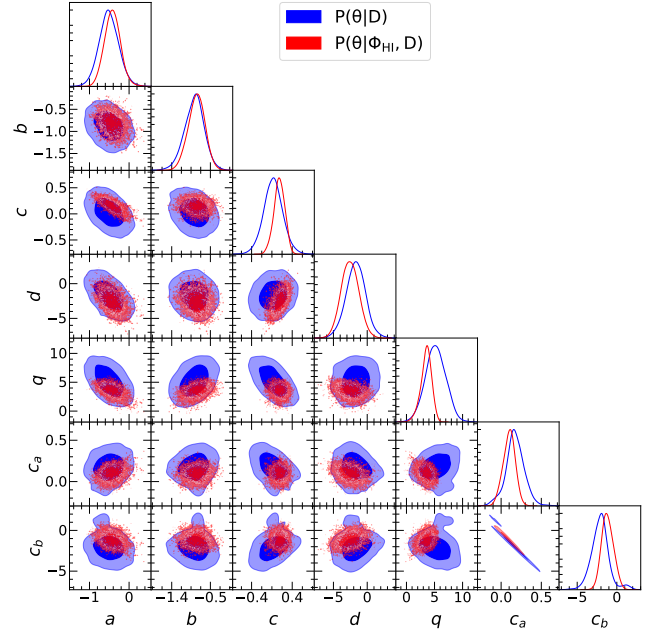


Figure 3. Probability distribution of model parameters. Contours correspond to $1\text{-}\sigma$ and $2\text{-}\sigma$ from inside out. The blue contours show the distribution of $P(\theta|\mathbf{D})$, and the red contours show the distribution of $P(\theta|\Phi_{\text{HI}}, \mathbf{D})$.

3.3. Tests with mock HI catalogs

Our HI mass estimator is not simply a predictor of the mean value for galaxies of a given set of optical properties (as usually the case in previous studies), but rather it includes the variance of individual galaxies. For an individual galaxy with real HI measurement, the estimated HI mass may be different from the real value because of the scatter. Therefore, we cannot directly compare the estimated and real values of the HI mass for individual galaxies in ALFALFA and xGASS. Instead, we can test our HI estimator only statistically, by comparing the predicted distribution of HI mass with that obtained from real observations. To facilitate a fair comparison, we also need mock catalogs constructed to include the same selection effects as xGASS or ALFALFA. If our HI estimator provides an unbiased HI prediction for a sample of general-population galaxies (rather than individual galaxies) selected from an optical survey, the mock catalog should reproduce the HI mass distribution obtained from the real sample.

From the ALFALFA α .100 sample, we select a 100% complete sample of 6198 HI-detected galaxies with $z < 0.05$ and $\log M_*/M_{\odot} > 9$, and in the sky area of $138^\circ < \alpha < 232^\circ$ and $0^\circ < \delta < 36.5^\circ$, the overlapping sky coverage of the SDSS and ALFALFA α .100 footprints. We require the lower mass limit of $\log M_*/M_{\odot} > 9$ in order to keep consistency with the mass limit of the calibration

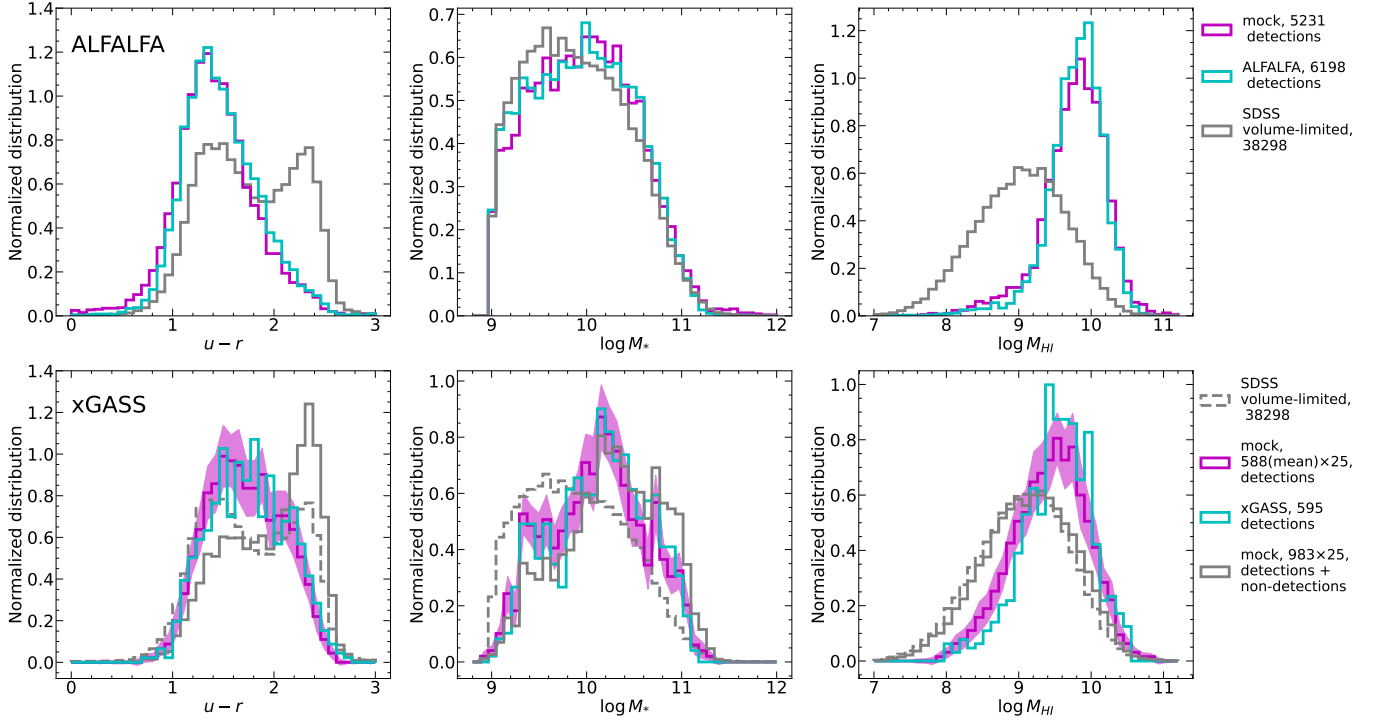


Figure 4. Normalized distribution of $u - r$, $\log M_*$ and $\log M_{\text{HI}}$ of galaxies. The cyan histogram represents the results of real samples and the magenta histogram of mock samples. Both the grey solid histogram in the top panel and the grey dashed histogram in the bottom panel represent the SDSS volume-limited sample used to construct ALFALFA mock catalog. The grey solid histogram in the bottom panel represents the mean distribution of the 25 mock xGASS samples. The magenta shaded area shows the $1 - \sigma$ scatter of the 25 mocks.

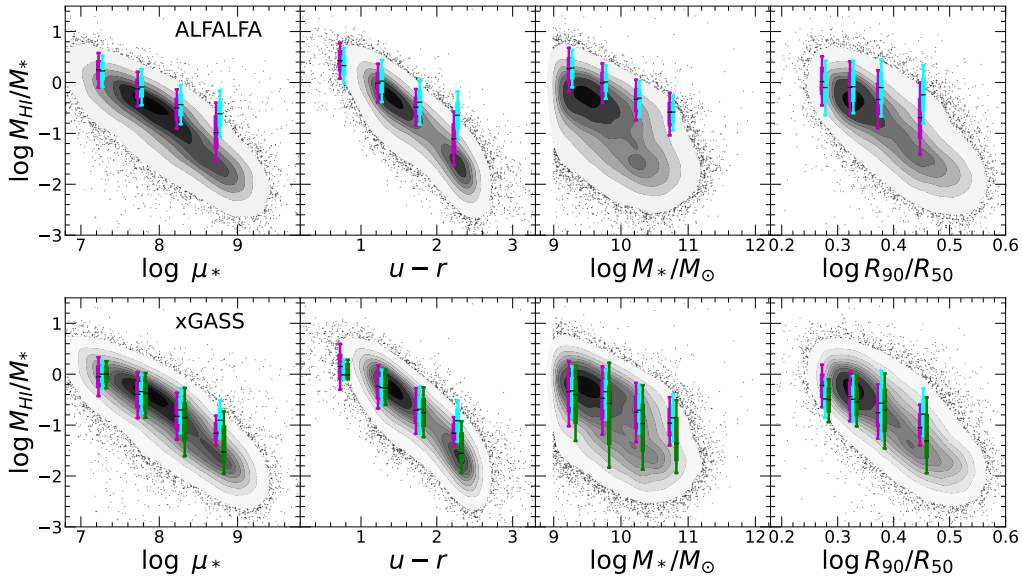


Figure 5. HI mass fraction as a function of galaxy properties for ALFALFA(top)/xGASS(bottom) mock and real survey. From left to right, the horizontal axis represents galaxy surface mass density, $u - r$ color index, stellar mass and galaxy concentration respectively. The y-axis is the observed HI mass fraction for HI-detected galaxies in real surveys and the estimated HI mass fraction for galaxies in mock surveys. The grey contours represent the volume-limited sample used in the mock ALFALFA survey. The contours include 5%, 15%, 25%, ..., 95% of the total sample. Galaxies outside these contours are shown as grey dots. The boxes show the 25% - 75% percentile range of galaxies detected in mock surveys (magenta) or real surveys (cyan) in each bin. The vertical error bars show the 5% - 95% percentile range. The green boxes show the distribution of the total xGASS sample (SampleX, detections + non-detections)

sample SampleX. In addition, galaxy samples selected

with $z < 0.05$ and $\log M_*/M_\odot > 9$ are actually volume-

limited, and so we do not need to worry about sample incompleteness when comparing our mock catalog with the ALFALFA sample. Using the ALFALFA 100% completeness limit is for the same consideration. The 100% completeness limit is obtained by extrapolating the 25%, 50% and 90% completeness limits derived by Haynes et al. (2011) using the distribution of ALFALFA extragalactic sources in the plane defined by the HI integrated flux density (S_{21}) and the line profile width (W_{50}). To construct the corresponding mock catalog, we start with a volume-limited sample of SDSS galaxies selected from `SampleS` that covers the same sky area, stellar mass and redshift ranges as the ALFALFA 100% complete sample. This volume-limited sample contains 38,298 galaxies. For each galaxy we then apply our $\log(M_{\text{HI}}/M_*)$ estimator to obtain an HI mass, and calculate S_{21} according to the estimated HI mass and the redshift of the galaxy. We estimate the line width W_{50} for the galaxy using the stellar mass Tully-Fisher relation given in Bloom et al. (2017) with inclination considered. Considering that the HI masses in the ALFALFA catalog are not corrected for HI self-absorption and for a fair comparison between our mock catalog and the ALFALFA sample, we have estimated an HI mass for the mock galaxy without applying the self-absorption correction. The galaxy is included in the mock catalog if its HI flux density is above the 100% detection limit corresponding to its flux density and line width. A total of 5231 galaxies are selected into the mock catalog.

For xGASS, we take all the 983 galaxies including 595 HI-detected galaxies with M_{HI}/M_* above a detection limit of 4%, and 388 non-detections below the limit. The detection threshold of the HI-to-stellar mass ratio is chosen to be slightly higher than the usually quoted limit of $\sim 1.5\%$ to ensure that the subsample of detections is truly complete down to the limit. We form a set of 25 mock catalogs, each constructed by randomly selecting 983 galaxies from `SampleS` in the same stellar mass and redshift ranges either as the GASS survey ($10.2 < \log M_*/M_\odot < 11.5$ and $0.025 < z < 0.05$) or as the extended xGASS survey ($9.0 < \log M_*/M_\odot < 10.2$ and $0.01 < z < 0.02$). In addition, we require each of the mock catalogs to follow the same stellar mass distribution as the xGASS sample. The mock galaxies with $M_{\text{HI}}/M_* > 4\%$ are taken as detections and others are non-detections. On average, the mock catalogs contain 588 detections, very close to the real sample (595).

In Figure 4 we compare the distribution of $u - r$, $\log M_*$ and $\log M_{\text{HI}}$ for the mock and real samples, with the upper and lower panels for ALFALFA and xGASS, respectively. The mock catalogs well reproduce the distribution of M_{HI} for HI-detected galaxies in both sur-

veys, indicating that our estimator is able to provide unbiased HI estimates for the general population of galaxies.

The mock catalog of ALFALFA also reproduces the distributions of $u - r$ and $\log M_*$ in the real sample. The distribution of the parent SDSS volume-limited sample used to construct the ALFALFA mock catalog is plotted in the upper panels for comparison. As expected, the ALFALFA detections are biased to relatively blue and HI-rich galaxies. The full sample of xGASS including both detections and non-detections show a similar distribution in $u - r$ (although with a slightly higher fraction of blue galaxies) and the same distribution in M_{HI} when compared to the SDSS volume-limited sample. This indicates that xGASS is a more representative sample of the general population, and thus more appropriate for calibrating the HI mass estimator, than ALFALFA.

In Figure 5 we plot the HI-to-stellar mass ratio as functions of μ_* , $u - r$, M_*/M_\odot and R_{90}/R_{50} for the real and mock catalogs. For the mock catalogs and the SDSS volume-limited sample the HI-to-stellar mass ratios are the values predicted by our estimator, while the observed values are plotted for real galaxies in ALFALFA and xGASS. The mock catalogs of HI-detected galaxies agree well with real HI samples for both surveys. When compared to the model predictions based on the SDSS volume-limited sample, the samples of detection from both surveys and the corresponding mock catalogs are biased for gas-rich galaxies, and this bias becomes more significant for galaxies with larger stellar mass, redder color, higher surface density, and more concentrated light distribution. When including both detections and non-detections (the green boxes), the xGASS mock catalogs closely follow the trend of the volume-limited sample, suggesting again that the xGASS survey represents well the general population of galaxies.

4. HI GAS CONTENTS IN GALAXIES AND IN DARK MATTER HALOS

4.1. The HI Mass Function of galaxies

Using the constrained HI mass estimator given above, we can predict the HI mass function (HIMF) starting from an optical sample. For this purpose we use the SDSS galaxy sample (`SampleS`) for which we have estimated an HI mass for each galaxy using the best model parameters and their dispersion. We use two different methods to estimate the HIMF, as detailed below.

In the first method, we use the $1/V_{\text{max}}$ -weighting scheme following Li & White (2009) and Chen et al. (2019) in their estimates of the stellar mass function of galaxies. For each galaxy i we determine $V_{\text{max},i}$, the to-

tal comoving volume of the survey out to the maximum redshift $z_{\max,i}$ at which the galaxy in question would meet the apparent magnitude criterion of our sample $r \leq 17.6$. Luminosity evolution and K -correction are included in the calculation of $z_{\max,i}$. The HIMF is then estimated as

$$\Phi(M_{\text{HI}})\Delta \log M_{\text{HI}} = \sum_i (f_{\text{sp},i} V_{\max,i})^{-1} \frac{\rho_{\text{u}}}{\rho(V_{\max,i})}, \quad (12)$$

where the sum runs over all galaxies with HI mass in the range $M_{\text{HI}} \pm 0.5\Delta \log M_{\text{HI}}$. Here $f_{\text{sp},i}$ is the spectroscopic completeness which varies across the survey area and is defined as the fraction of photometrically-selected targets that are spectroscopically observed and included in our sample. The last term in the equation $\rho_{\text{u}}/\rho(V_{\max,i})$ is the ratio of the average mass density within the whole survey volume to that within $V_{\max,i}$, as determined in [Chen et al. \(2019\)](#) based on the ELUCID simulation ([Wang et al. 2014](#)), a constrained simulation in the SDSS volume, in order to account for the effect of cosmic variance caused by the limited sample volume at low redshift.

In the second method, we first estimate the r -band luminosity function (LF) from `SampleS`, $\phi(M_r)$, using the same $1/V_{\max}$ -weighting scheme as described above. We then divide all galaxies in `SampleS` into a successive sequence of non-overlapping M_r bins, $M_{r,k} \leq M_r < M_{r,k+1}$ ($k = 1, \dots, N_m$), with a fixed logarithmic interval of $\log(M_{r,k+1}/M_{r,k}) = 0.2$ dex. For the k -th interval we obtain the HI mass distribution of sample galaxies $\Psi_k(M_{\text{HI}} \pm 0.5\Delta M_{\text{HI}})$, normalized so as to have $\sum \Psi_k \Delta M_{\text{HI}} = 1$. The HIMF of the whole sample can then be estimated as

$$\Phi(M_{\text{HI}}) = \sum_{k=1}^{N_m} \left[\Psi_k(M_{\text{HI}}) \int_{M_{r,k}}^{M_{r,k+1}} \phi(M_r) dM_r \right], \quad (13)$$

where the sum runs over all the absolute magnitude bins for a given HI mass range $M_{\text{HI}} \pm 0.5\Delta M_{\text{HI}}$. In principle the two methods should lead to identical results. The advantage of the second one is that the complex selection effects of the galaxy sample are already accounted for when estimating the LF, so that one can obtain the HIMF simply by counting the sample galaxies in bins of M_{HI} . This method is valid only when the sample galaxies at a given luminosity are not biased in their HI mass distribution. This should be true for an optically-selected sample like the SDSS that does not involve any HI-related selections. We use the LF estimated from `SampleS` by ourselves, not only for self-consistency but also to take advantage of the $1/V_{\max}$ weights given in [Chen et al. \(2019\)](#) with corrections for the cosmic variance effect in the local universe.

Table 1. Schechter function parameters of CHIMFs

$\log(M_{200}/M_{\odot})$	Φ_{HI}^*	$\log M_{\text{HI}}^*$	α
All galaxies:			
[12.00, 12.34)	0.34 ± 0.04	10.13 ± 0.04	-1.17 ± 0.05
[12.34, 12.68)	0.26 ± 0.02	10.29 ± 0.03	-1.41 ± 0.02
[12.68, 13.03)	0.31 ± 0.02	10.34 ± 0.02	-1.54 ± 0.02
[13.03, 13.37)	0.92 ± 0.11	10.14 ± 0.04	-1.42 ± 0.03
[13.37, 13.71)	2.55 ± 0.24	9.99 ± 0.04	-1.23 ± 0.03
[13.71, 14.05)	2.79 ± 0.32	10.15 ± 0.03	-1.50 ± 0.04
[14.05, 14.39)	8.66 ± 1.10	9.99 ± 0.04	-1.41 ± 0.03
[14.39, 14.73)	8.85 ± 1.09	10.09 ± 0.04	-1.56 ± 0.03
[14.73, 15.08)	26.99 ± 3.15	10.09 ± 0.03	-1.53 ± 0.03
Red galaxies:			
[12.00, 12.34)	0.10 ± 0.02	9.84 ± 0.06	-1.45 ± 0.06
[12.34, 12.68)	0.17 ± 0.03	10.01 ± 0.05	-1.43 ± 0.05
[12.68, 13.03)	0.16 ± 0.02	10.22 ± 0.03	-1.59 ± 0.03
[13.03, 13.37)	0.31 ± 0.06	10.19 ± 0.06	-1.51 ± 0.04
[13.37, 13.71)	0.89 ± 0.13	10.00 ± 0.06	-1.28 ± 0.04
[13.71, 14.05)	0.55 ± 0.09	10.29 ± 0.05	-1.68 ± 0.04
[14.05, 14.39)	3.75 ± 0.81	9.97 ± 0.06	-1.46 ± 0.05
[14.39, 14.73)	3.56 ± 0.71	10.11 ± 0.06	-1.69 ± 0.05
[14.73, 15.08)	9.02 ± 2.05	10.16 ± 0.06	-1.71 ± 0.05
Blue galaxies:			
[12.00, 12.34)	0.30 ± 0.05	10.13 ± 0.06	-1.02 ± 0.07
[12.34, 12.68)	0.22 ± 0.03	10.21 ± 0.05	-1.26 ± 0.05
[12.68, 13.03)	0.19 ± 0.01	10.36 ± 0.02	-1.45 ± 0.01
[13.03, 13.37)	0.66 ± 0.05	10.09 ± 0.03	-1.34 ± 0.02
[13.37, 13.71)	1.72 ± 0.12	9.97 ± 0.02	-1.19 ± 0.02
[13.71, 14.05)	2.76 ± 0.22	10.03 ± 0.03	-1.30 ± 0.03
[14.05, 14.39)	5.23 ± 0.40	9.98 ± 0.02	-1.35 ± 0.03
[14.39, 14.73)	6.33 ± 0.49	10.03 ± 0.03	-1.36 ± 0.02
[14.73, 15.08)	23.48 ± 1.42	9.96 ± 0.02	-1.21 ± 0.02
Satellite galaxies:			
[12.00, 12.34)	0.06 ± 0.01	10.02 ± 0.02	-1.65 ± 0.03
[12.34, 12.68)	0.14 ± 0.02	10.04 ± 0.03	-1.63 ± 0.03
[12.68, 13.03)	0.24 ± 0.02	10.10 ± 0.03	-1.67 ± 0.03
[13.03, 13.37)	0.79 ± 0.08	10.04 ± 0.03	-1.49 ± 0.03
[13.37, 13.71)	2.23 ± 0.18	9.95 ± 0.03	-1.27 ± 0.03
[13.71, 14.05)	2.82 ± 0.27	10.09 ± 0.03	-1.51 ± 0.04
[14.05, 14.39)	8.37 ± 1.07	9.97 ± 0.04	-1.42 ± 0.04
[14.39, 14.73)	8.58 ± 1.00	10.08 ± 0.03	-1.58 ± 0.03
[14.73, 15.08)	27.34 ± 3.05	10.08 ± 0.03	-1.53 ± 0.03

NOTE— Φ_{HI}^* , M_{HI}^* , and α are the characteristic amplitude, characteristic mass and the low-mass end slope of a Schechter function. In the last two halo bins, there is nearly no blue central galaxies so no fitting parameters are given.

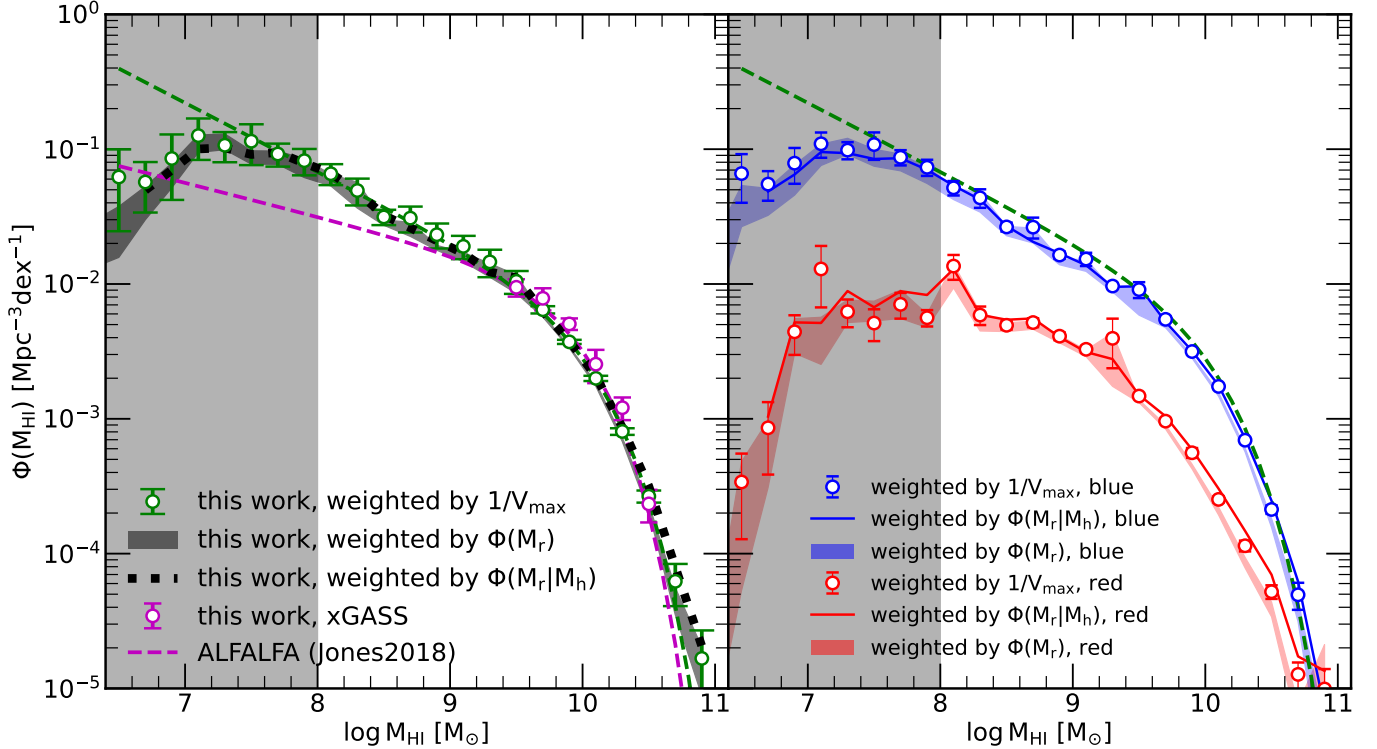


Figure 6. The HI mass function of galaxies. Left panel: The HI mass function of all galaxies in the local universe. The green open circles with errorbars are the results of this work using $1/V_{\max}$ weighting method. The green dashed line is the fit to the green circles. The dark shaded region shows the HIMF derived from our luminosity function. The thick dark dashed line is the HIMF derived from conditional luminosity function (see subsection 5.2). The magenta dashed line and open circles are the results of ALFALFA and xGASS (see subsection 3.2). The grey shaded region indicates the HI mass regime where `SampleS` is incomplete and so the HIMF (green symbols) can only be considered as lower limits of the true HIMF. Right panel: the HI mass function of red and blue galaxies. The open circles are derived from $1/V_{\max}$ method. The colored areas are derived from luminosity function. The solid lines are derived from conditional luminosity function.

In the left panel of Figure 6, we show the HIMF derived for our sample using the two methods described above, with green circles with error bars for the first method and the grey-shaded band for the second method. The errors of the HIMF from both methods are estimated using the bootstrap re-sampling method, which accounts for uncertainties due to sampling, but does not include the cosmic variance and uncertainties in the HI mass estimate. As expected, the HIMFs from the two methods are in good agreement with each other over the entire mass range. The HIMF increases as one goes from high to low M_{HI} but at $M_{\text{HI}} \sim 10^8 M_{\odot}$ the HIMF flattens and even decreases slightly towards the low-mass end. This behavior at the low-mass end is not real, but caused by the incompleteness of the SDSS sample at stellar masses below $M_* \sim 10^8 M_{\odot}$, corresponding to a mean HI mass of $M_{\text{HI}} \sim 10^8 M_{\odot}$ according to our HI mass estimator. Thus, our HIMF at $M_{\text{HI}} < 10^8 M_{\odot}$ should be taken as a ‘lower limit’. We fit our HIMF at $M_{\text{HI}} > 10^8 M_{\odot}$ with a single Schechter function (Schechter 1976) and plot the result as the dashed

green line in Figure 6. The parameters of the fit are $\Phi_{\text{HI}}^* = 2.61 \pm 0.2 \times 10^{-3} \text{Mpc}^{-3} \text{dex}^{-1}$, $\log M_{\text{HI}}^*/M_{\odot} = 10.07 \pm 0.02$, and $\alpha = -1.51 \pm 0.02$. Integrating the best fit of our HIMF gives the cosmic density of the HI gas locked in local galaxies: $\Omega_{\text{HI}} = 4.1 \pm 0.1 \times 10^{-4}$, which is 17% and 5% higher than that from HIPASS (Zwaan et al. 2005) and ALFALFA (Jones et al. 2018a), respectively. For comparison we plot the Schechter function fit of the ALFALFA HIMF derived by Jones et al. (2018a) and the xGASS HIMF derived by us in subsection 3.2. We note that we have corrected the self-absorption effect for the estimated HI masses in order for an HIMF estimate that is as close as possible to the true HIMF of the local Universe. Our tests showed that the self-absorption correction has a median value of < 0.03 dex, and so it should make little difference in the HIMF. Therefore, the comparison with the ALFALFA HIMF still makes sense, although the ALFALFA HIMF is based on uncorrected HI masses. The HIMF estimated from the optical sample agrees well with both the ALFALFA and xGASS HIMFs at $\log M_{\text{HI}} > 9.5$ where we

Table 2. Gaussian function parameters of CHIMFs

$\log(M_{200}/M_{\odot})$	Φ_{HI}^*	σ	$\log M_{\text{HI}}^*$
Central galaxies:			
[12.00, 12.34)	0.606 ± 0.017	0.479 ± 0.010	8.877 ± 0.013
	0.369 ± 0.024	0.391 ± 0.016	9.714 ± 0.026
[12.34, 12.68)	0.742 ± 0.024	0.460 ± 0.010	9.072 ± 0.016
	0.217 ± 0.021	0.360 ± 0.020	9.810 ± 0.037
[12.68, 13.03)	0.794 ± 0.032	0.455 ± 0.009	9.271 ± 0.021
	0.165 ± 0.009	0.442 ± 0.014	9.932 ± 0.024
[13.03, 13.37)	0.851 ± 0.029	0.444 ± 0.007	9.371 ± 0.017
	0.107 ± 0.009	0.467 ± 0.016	9.940 ± 0.041
[13.37, 13.71)	0.867 ± 0.024	0.451 ± 0.006	9.445 ± 0.014
	0.099 ± 0.007	0.443 ± 0.026	10.013 ± 0.034
[13.71, 14.05)	0.895 ± 0.022	0.457 ± 0.007	9.559 ± 0.011
	0.072 ± 0.010	0.573 ± 0.024	10.012 ± 0.069
[14.05, 14.39)	0.921 ± 0.037	0.453 ± 0.009	9.615 ± 0.016
	0.016 ± 0.001	0.419 ± 0.033	10.051 ± 0.041
[14.39, 14.73)	0.930 ± 0.054	0.412 ± 0.015	9.686 ± 0.024
	—	—	—
[14.73, 15.08)	0.948 ± 0.063	0.425 ± 0.019	9.719 ± 0.028
	—	—	—

NOTE— Φ_{HI}^* , M_{HI}^* , and σ are the amplitude, center and width of a Gaussian profile. For each halo bin the CHIMF of central galaxies are fitted with two Gaussians, corresponding to the two rows of parameters in the table (The first row for red and the second row for blue).

have all the HIMF estimates available. At lower masses our HIMF differs from that of ALFALFA in that it has increasingly higher amplitudes and a steeper slope as the HI mass decreases from $M_{\text{HI}} \sim 10^9 M_{\odot}$ down to $M_{\text{HI}} \sim 10^8 M_{\odot}$. The difference is a factor of about 2 at $M_{\text{HI}} \sim 10^8 M_{\odot}$.

In the right panel of Figure 6 we show the HIMF derived in the same way, but separately for red and blue galaxies. For this purpose we have classified each galaxy in `SampleS` as red or blue according to the luminosity-dependent $u-r$ color demarcation given by Baldry et al. (2004). As can be seen, the two methods provide very consistent results even when galaxies are divided into red and blue subsamples. The HIMF of the blue galaxy population is higher than that of the red population over the entire M_{HI} range except for the largest masses where the amplitudes of the two HIMFs become comparable. Clearly, the total HIMF of all galaxies is dominated by blue galaxies.

4.2. The conditional HI Mass Function

The second statistic we can predict is the conditional HI mass function (CHIMF), $\Phi(M_{\text{HI}}|M_h)$, which is the HIMF of galaxies hosted by dark matter halos of a given mass M_h . A number of studies have previously attempted to obtain the HIMF of galaxies in groups/clusters based on HI observations of a small number of nearby groups (e.g. Freeland et al. 2009; Kilborn et al. 2009; Pisano et al. 2011), or for individual systems in the local Universe such as the Leo I group (Stierwalt et al. 2009), the Sculptor group (Westmeier et al. 2017) and the Virgo cluster (Jones et al. 2018b). Based on the SDSS group catalog and the ALFALFA survey Jones et al. (2020) have recently obtained HIMFs for galaxy groups in three halo mass bins. Taking advantage of both the large and complete galaxy sample from the SDSS and the unbiased HI masses estimated with our estimator, here we perform a first attempt to obtain the CHIMFs for narrow ranges of dark matter halo mass and down to substantially low M_{HI} , as well as for red/blue galaxies and central/satellite galaxies separately.

We adopt the second method described in subsection 4.1 to estimate the CHIMFs, except that we use the conditional luminosity function (CLF; $\phi(M_r|M_h)$) instead of the total LF in Equation 13. The CLFs of galaxies in the local Universe were estimated by Lan et al. (2016, hereafter Lan16) based on the SDSS galaxy group catalog (Yang et al. 2007) and the SDSS photometric sample down to a r -band absolute magnitude of $M_r = -12$. Lan16 considered a number of halo mass bins ranging from $M_h \sim 10^{12} M_{\odot}$ up to $\sim 10^{15} M_{\odot}$. For each of the bins they obtained the CLFs separately for red and blue galaxies (divided by a luminosity-dependent $u-r$ color demarcation), as well as for central and satellite galaxies (with the central/satellite classification provided by the SDSS group catalog). Correspondingly, we estimate the CHIMFs for red/blue and central/satellite galaxies separately, applying the same color cut and central/satellite classification as in Lan16 to divide our sample galaxies into red/blue or central/satellite subsamples. We divide galaxies of a given subsample into bins of M_r . The CHIMF for the subsample in each halo mass bin, $\Phi(M_{\text{HI}}|M_h)$, is then given by Equation 13, where the LF is replaced by the corresponding CLF $\phi(M_r|M_h)$. We note that we have adopted a luminosity limit of $M_r = -14.4$ when estimating the CHIMFs, to avoid large uncertainties caused by the rather noisy distributions of M_{HI} at lower luminosities.

In Figure 7 we show the CHIMFs of red/blue and central/satellite galaxies as well as the total CHIMF, for different halo mass bins as indicated in each panel.

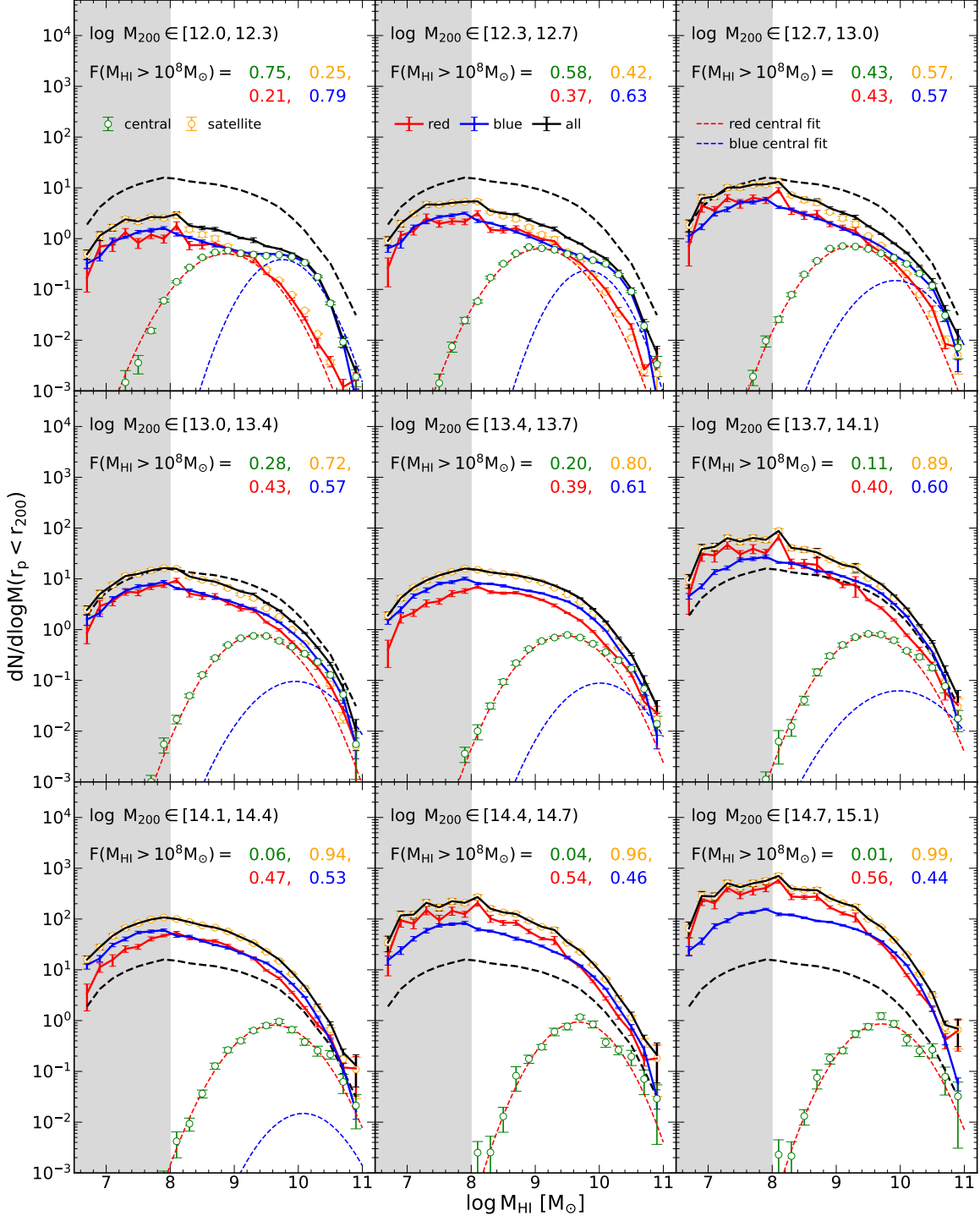


Figure 7. Conditional HI mass function. The orange and green open circles represent the CHIMFs of satellites and centrals respectively. The black solid lines represent the CHIMFs of all galaxies. For comparison, the CHIMF of all galaxies in halos of $\log M_h \in [13.4, 13.7]$ is plotted as the black dashed line in each panel. The red and blue solid lines are the CHIMFs of red and blue galaxies. The fitting result of central galaxies is shown as red and blue dashed lines for red and blue central galaxies. The colored numbers in each panel shows the contribution of central (green)/satellite (orange)/red (red)/blue (blue) galaxies to the total HI mass, calculated using corresponding CHIMFs above $M_{\text{HI}} > 10^8 M_{\odot}$. The grey shaded region shows the HI mass range where the CHIMFs suffer from incompleteness.

The total CHIMF of the halo mass bin of $13.37 \leq \log(M_h/M_\odot) < 13.71$ is repeated as the dashed black line in each panel for reference. From the CHIMFs we calculate the fraction of the total HI mass in dark halos of given mass as contributed by red, blue, central and satellite galaxies with $M_{\text{HI}} > 10^8 M_\odot$. These mass fractions are indicated in each panel with different colors for different types of galaxies. A Schechter function can well describe all the HIMFs except those for central galaxies where a double Gaussian profile provides a better description for low-mass halos and a single Gaussian profile works better for high-mass halos. When divided into red and blue subsamples, central galaxies at fixed halo mass can each be modeled by a single Gaussian, as is shown in the figure where red and blue dashed lines are the Gaussian fits of red and blue centrals, respectively. The Schechter function parameters for the total sample and the subsamples of red, blue and satellite galaxies in each halo mass bin are listed in Table 1, while the parameters of the two Gaussian functions for sub-samples of central galaxies are listed in Table 2.

As can be seen from Figure 7, the amplitude of the total HIMF increases monotonically with increasing halo mass, indicating a positive correlation of the total HI mass of galaxies with the dark matter mass of their host halos. The low-mass slope of the total HIMF in Milky Way-like halos ($M_h \sim 10^{12} M_\odot$) is relatively flat with $\alpha = -1.17$, which is consistent with previous works where $\alpha \lesssim -1.2$ was found for nearby groups hosted by dark halos of similar mass (e.g. Freeland et al. 2009; Kilborn et al. 2009; Pisano et al. 2011; Westmeier et al. 2017; Jones et al. 2020). As halo mass increases, the low-mass slope becomes steeper, reaching a slope index of $\alpha < -1.5$ at the highest halo mass (see Table 1). Jones et al. (2020) also attempted to measure the HIMFs for SDSS galaxy groups of $M_h > 13h^{-1} M_\odot$ using the ALFALFA survey, finding flat slopes at the low-mass end similar to groups of lower masses. As those authors pointed out, however, their low-mass slope was well sampled only for groups at $M_h < 10^{13} M_\odot$ and the measurements at higher masses were uncertain due to the limited depth of the ALFALFA survey. In addition, from Table 1 we find the characteristic mass M_{HI}^* of the Schechter function for the total HIMF to span a narrow range of $M_{\text{HI}}^* \sim 1 - 2 \times 10^{10} M_\odot$. This result is consistent with early studies which found weak dependence of the turnover mass of galaxy HIMFs on environmental density (e.g. Moorman et al. 2014; Jones et al. 2016).

When galaxies are divided by color, we find that the red and blue populations present similar CHIMFs for halos of different masses, in terms of both amplitude and shape, which results in a comparable HI mass frac-

tion for the two populations in halos of different masses. Quantitatively, the HI mass fraction in red (blue) galaxies increases (decreases) steadily from 21% (79%) at $M_h \sim 10^{12} M_\odot$ to 56% (44%) at $M_h \sim 10^{15} M_\odot$. It has been well established that blue galaxies dominate the central galaxy population in intermediate-to-low mass halos, and red galaxies are either (massive) centrals in massive halos or (less-massive) satellites in halos of different masses (Yang et al. 2009; Lan et al. 2016). Thus, massive halos are expected to contain more red galaxies than blue galaxies. The fact that red and blue galaxies have comparable CHIMFs at given halo mass can be understood from the color-dependent HI-to-stellar mass ratio of galaxies, which is smaller for redder galaxies.

For central galaxies, the CHIMFs appear to depend weakly on halo mass, with the average M_{HI} increasing slightly and the width decreasing slightly with increasing halo mass. The two Gaussian components correspond to contributions by central galaxies of red and blue colors, respectively. Blue centrals contribute significantly to the total HI of the central galaxy population only in low-mass halos, with a contribution that is comparable to that of red centrals in Milky Way-like halos and declines with halo mass. At $M_h \gtrsim 10^{14} M_\odot$, the CHIMF of centrals is dominated by red galaxies, with a negligible contribution from blue centrals. Central galaxies as a whole contribute a significant amount of HI mass only in low-mass halos, with a fraction of 75% and 58% in the two lowest-mass halo bins, respectively, and the fraction decreases rapidly at larger halo masses, becoming less than 10% when the halo mass exceeds $M_h \sim 10^{14} M_\odot$. In contrast to centrals, the satellite galaxy population has a Schechter CHIMF that varies with halo mass in a way similar to the total CHIMF. Consequently, the satellite population contributes a larger fraction of the total HI mass as the halo mass increases. We would like to point out that, this result is not in conflict with the known fact that HI-selected galaxy samples in the local Universe are dominated by field central galaxies (Martin et al. 2012; Papastergis et al. 2013; Guo et al. 2017). This is because our CHIMFs are limited to relatively massive halos with $M_h > 10^{12} M_\odot$, while field centrals are predominantly found in halos of lower masses. The total HI budget of the galaxy population should be dominated by low-mass halos according to the power-law shape of the halo mass function.

4.3. The HI-halo mass relation

One can obtain the total HI mass locked in member galaxies in dark matter halos by integrating the CHIMFs derived above. The result is shown as dashed lines in Figure 8, where we plot the total HI mass

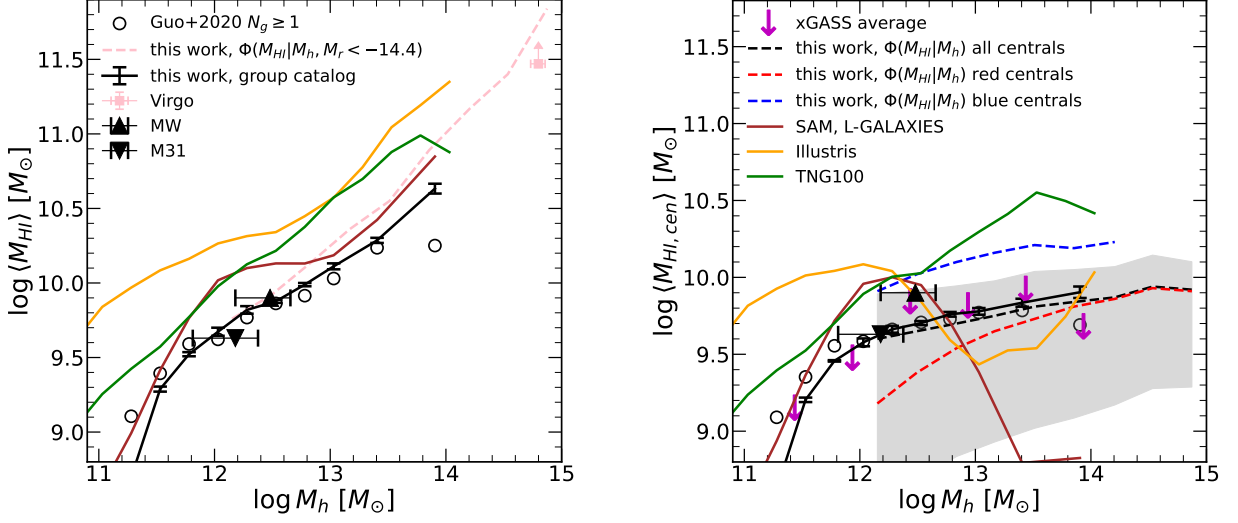


Figure 8. The left panel shows the average HI mass of dark matter halos and the right panel shows the average HI mass of central galaxies. In both panels, the black open circles are the result of Guo et al. (2020) in $N_g \geq 1$ case. For central galaxies, they have been corrected for the confusion effect using our estimator. The black solid line is our result derived from group catalog. The brown, orange and green solid lines represent the result of L-GALAXIES semi-analytical model, Illustris simulation and IllustrisTNG simulation, respectively. The black upward and downward triangles represent the Milky Way and M31, respectively. In the left panel, the pink dashed line is the result of our CHIMF and the pink upward arrow with error bars represents Virgo Cluster. In the right panel, the black dashed line is the average central HI mass derived from our CHIMFs, and the grey shaded region represents the 16% to 84% percentile of the central CHIMFs in each halo mass bin. The red and blue dashed lines are the mean HI mass of red and blue central galaxies from our CHIMFs. The magenta downward arrows represent the upper limit of HI masses of central galaxies in xGASS sample.

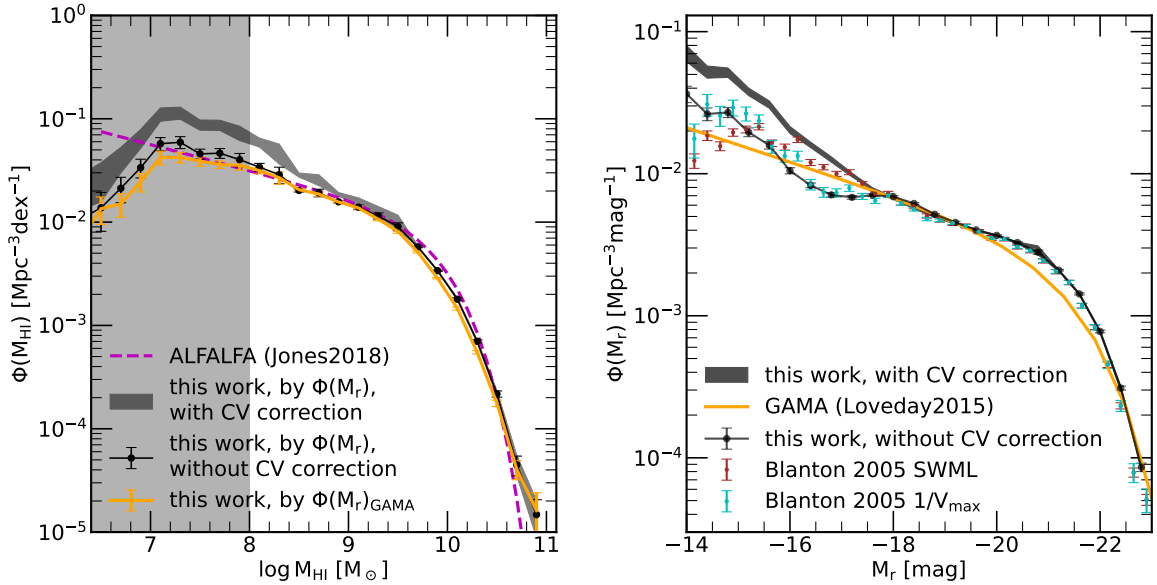


Figure 9. Left panel: the HI mass function. The magenta dashed line is ALFALFA's result. The orange solid line is derived from GAMA LF. The black shaded region and solid line are derived from our LF with and without CV correction respectively. The grey shaded region shows the mass range suffering from sample incompleteness. Right panel: the orange solid line is the GAMA LF. The brown and cyan points with errorbars represent the LF of (Blanton et al. 2005) derived by SWML and $1/V_{\text{max}}$ method respectively. The dark region and points show our LF with and without CV correction.

in all galaxies (left panel) and central galaxies (right panel) as a function of halo mass. The total HI mass of all galaxies increases monotonically with halo mass, from $M_{\text{HI}} \sim 8 \times 10^9 M_{\odot}$ for Milky Way-like halos with $M_{\text{h}} \sim 10^{12} M_{\odot}$ up to $M_{\text{HI}} \sim 7 \times 10^{11} M_{\odot}$ for Coma-like halos with $M_{\text{h}} \sim 5 \times 10^{14} M_{\odot}$. The total HI mass in central galaxies shows a rather weak dependence on halo mass, with M_{HI} slightly increasing from $\sim 4 \times 10^9 M_{\odot}$ to $\sim 8 \times 10^9 M_{\odot}$.

The HI-to-halo mass (HIHM) relation can also be estimated from a galaxy group catalog (Lim et al. 2017) for which we have estimated the HI mass for each galaxy using our estimator. To that end, we divide galaxy groups into a set of halo mass bins, and for groups in each bin we sum up the HI mass of all member galaxies (or central galaxies) to obtain the HIHM relation for all galaxies (or central galaxies). Each galaxy is weighted in the same way as in Equation 12 in order to correct for the sample incompleteness and cosmic variance effect. The relations derived this way are plotted as the solid black lines in Figure 8 over the range from $M_{\text{h}} \sim 10^{11} M_{\odot}$ to $M_{\text{h}} \sim 5 \times 10^{13} M_{\odot}$. The error bars are estimated from the scatter among 20 bootstrap samples. For central galaxies, the HIHM relation derived from the group catalog is consistent with the average relation derived from the CHIMFs. For all galaxies as a whole, however, the relation derived from the group catalog agrees with the CHIMF-based result only at $M_{\text{h}} \sim 1-2 \times 10^{12} M_{\odot}$. Above this mass, the group catalog gives lower HI mass, and the difference increases with halo mass, reaching ~ 0.3 dex at $M_{\text{h}} \sim 5 \times 10^{13} M_{\odot}$. Possible reasons for this difference will be discussed in the next section.

The HIHM relations estimated from the group catalog are in good agreement with those of Guo et al. (2020) obtained by stacking the ALFALFA datacubes, as shown by open circles in Figure 8. We have corrected the confusion effect for the average M_{HI} mass of central galaxies measured by Guo et al. (2020) by subtracting the contribution of satellite galaxies that reside near their central galaxy. Following Guo et al. (2020), we use an angular aperture of $\max\{200\text{kpc}/D_A, 8'\}$ and a maximum velocity separation of 300 km s^{-1} to define the nearness. For comparison, the left panel of the same figure shows the total HI mass for the Milky Way (Kalberla & Kerp 2009), M31 (Chemin et al. 2009) and the Virgo Cluster. The HI mass of the Virgo Cluster is estimated by ourselves by applying our HI estimator to the Extended Virgo Cluster Catalog (EVCC; Kim et al. 2014). We only use galaxies in EVCC that are brighter than $M_r = -14.4$, corresponding to the luminosity limit adopted above for our CHIMFs, and are classified to be member galaxies of the Virgo Cluster based on the

spherical symmetric infall model (Praton & Schneider 1994). Thus, the resulting HI mass should perhaps be considered as a lower limit of the total HI mass in the cluster, as some HI may be contained in galaxies that are not included in our estimate. Observationally, Jones et al. (2018b) measured the HIMF of Virgo Cluster using ALFALFA data. Integrating the Virgo HIMF of the "extended Virgo cluster sample" in their work and assuming a spherical volume with a radius of 3 Mpc gives an HI mass of $\log M_{\text{HI}}(\text{Virgo})/M_{\odot} \sim 11.14$, about 0.3 dex lower than our result. However, we emphasize that since the definitions of Virgo galaxy sample used in these two works are quite different, this comparison is actually unfair. It is hard to tell whether our HI estimation of Virgo Cluster is consistent with Jones et al. (2018b) or not. Using central galaxies in `SampleX` we can also estimate the average HIHM relation, which is shown in the right-hand panel 8. We have included both detections and non-detections in this estimation, and so the HI masses from xGASS should be regarded as upper limits. As one can see, our HIHM relations are in broad agreement with all these previous measurements based on real observations of the HI gas, indicating that our estimator is reliable also for member galaxies of groups.

5. DISCUSSION

5.1. HIMF at the low mass end

Figure 6 shows that the HIMFs predicted by our estimator are higher and steeper than the HIMF obtained from ALFALFA at masses below a few $\times 10^9 M_{\odot}$. This discrepancy is predominantly caused by cosmic variance, which is corrected in our HIMFs but not in the ALFALFA result. The cosmic variance is taken into account through the last term of Equation 12, which was carefully determined by Chen et al. (2019) based on the ELUCID simulation, a constrained simulation with initial conditions that are reconstructed to reproduce the dark matter density field in the SDSS volume (Wang et al. 2014). The local volume within $z \sim 0.03$ has a density that is lower than the mean density of the universe. Consequently, the SDSS under-represents faint galaxies in the universe because it can detect these galaxies only at the very low redshift. ALFALFA is also limited to very low redshift, and so is also affected by the cosmic variance.

The effect of cosmic variance is shown clearly in Figure 9. In the right-hand panel, we show the r -band luminosity functions (LFs), $\Phi(M_r)$, estimated from `SampleS` with and without the cosmic variance correction, and compare them with the LFs obtained by Blanton et al. (2005) using an early SDSS sample, and with the LF obtained by Loveday et al. (2015) using the GAMA sur-

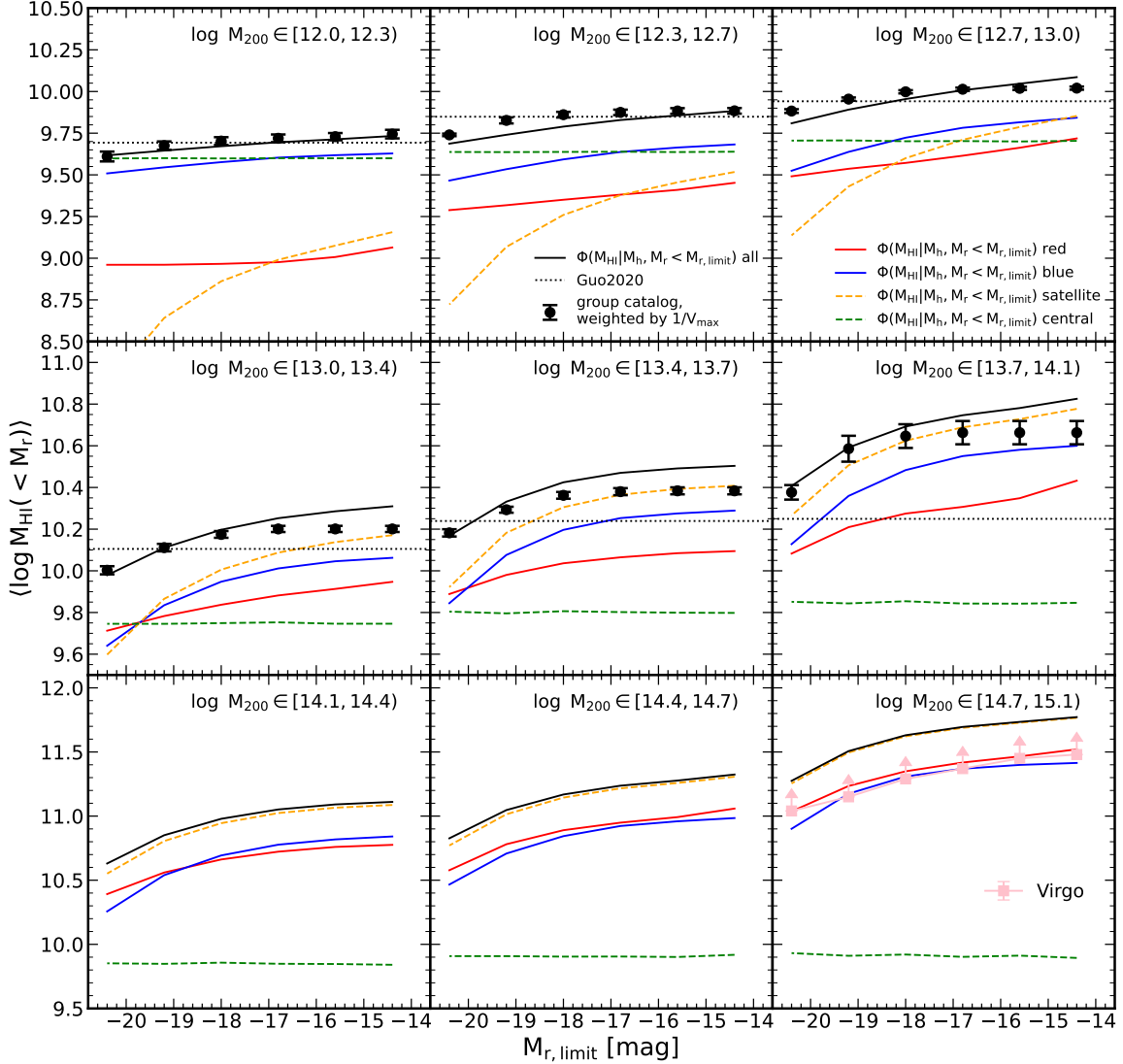


Figure 10. The HI mass in dark matter halos under different luminosity limits. In each panel, the black points represent the average HI mass of all galaxies in halos derived using group catalog. The horizontal black dotted line shows the result of (Guo et al. 2020). The red/blue/green/orange lines represent the HI mass in red/blue/central/satellite galaxies from our CHIMFs. The pink upward arrows show the result in the Virgo Cluster.

vey (Driver et al. 2011). The latter two studies did not correct for the cosmic variance effect, and it is not surprising that their LFs are flatter and lower than our measurements at the faint end. Our LF without including the cosmic variance correction shows a similarly lower amplitude at the low-mass end, confirming the importance of cosmic variance in the local universe. As pointed out in Blanton et al. (2005), the dip at $M_r \sim -17$ and the upturn at the faint end seen both in our uncorrected LF and the LF of Blanton et al. (2005) (the one estimated with the $1/V_{\text{max}}$ method) are produced by cosmic variance caused by the presence of large-scale structure in the sample volume, as the $1/V_{\text{max}}$ method is not capable of correcting such vari-

ance. The LF of Blanton et al. (2005) estimated using the step-wise maximum likelihood does not show such fluctuations at the faint end and is more consistent with the GAMA LF, but both are still lower than our LF corrected for the cosmic variance. In the left-hand panel of Figure 9 we compare the HIMFs derived with Equation 13, using our LFs with and without cosmic variance correction, as well as using the GAMA LF. The HIMFs without the correction are in good agreement with the ALFALFA result, demonstrating that the difference in the low-mass end between our corrected HIMF and the ALFALFA result is produced by the different treatments of the cosmic variance effect.

5.2. Conditional HI mass functions

As demonstrated in subsection 3.3, our HI-to-stellar mass estimator reproduces well the statistical properties of the mock catalogs that have the same selection effects as ALFALFA and xGASS. The application of our estimator to the SDSS sample also yields HIMFs that are in good agreement with the ALFALFA HIMF. All these indicate that our predicted CHIMFs are reliable. As a further test, we combine our CHIMFs for different halo masses to predict a total HIMF and compare it with the HIMFs estimated using other methods. The black dashed line in the left panel of Figure 6 shows the HIMF obtained from the sum of CHIMFs of different halo mass bins, each weighted by the number density of halos in the halo mass bin calculated using the halo mass function from Driver et al. (2022). Since the CHIMFs can be estimated only down to Milky Way-size halos with $M_h \sim 10^{12} M_\odot$ due to the mass limit in the SDSS group catalog, we have included the contribution of halos of lower masses following the method described in Lan et al. (2016). As can be seen from the figure, the HIMF estimated from the CHIMFs agrees very well with the HIMFs obtained with other methods.

As we have shown, the Schechter function provides a good description for the CHIMFs of all/red/blue/satellite populations in halos of different masses, while a double Gaussian function is suitable for central galaxies (see Table 1 and Table 2). These results have important implications for models of galaxy formation. For instance, a recent study by Li et al. (2022) used the HI-to-halo mass relation and clustering of HI galaxies obtained by Guo et al. (2017) and Guo et al. (2020) to constrain empirical models of the HI-halo relation by assuming that the HI mass of galaxies depends only on dark matter halo mass plus a secondary halo property, such as halo formation time and concentration. Their best-fit model predicts CHIMFs that have a log-normal form, quite different from the Schechter function found here (Figure 7). This implies that the model must have missed some key ingredients that regulate the HI gas content of galaxies. Our HI estimator involves four parameters, among which the stellar mass and color may be modeled by halo mass and formation time (see Wechsler & Tinker 2018, for a review). The other two parameters, surface stellar mass density and concentration, characterize the structure of galaxies and have been found to depend weakly on environments and properties of their host halos (e.g. Li et al. 2006; Blanton & Moustakas 2009). On the other hand, the HI mass fraction of galaxies may be stripped by environmental processes operating in dense regions, such as tidal stripping and ram-pressure stripping (e.g.

Gunn & Gott 1972; Cowie & Songaila 1977; Nulsen 1982; Boselli & Gavazzi 2006; Wang et al. 2021, 2022). These effects are expected to depend on both the stellar mass and surface mass density of galaxies (e.g. Li et al. 2012; Zhang et al. 2013). It is thus likely that physical processes related to both galaxy structure and environments may also play a role in determining HI gas contents of galaxies.

When divided according to color, red and blue central galaxies follow a Gaussian CHIMF, rather than a Schechter function (Figure 7). This is similar to the conditional stellar mass (or luminosity) function of central galaxies found in previous studies (e.g. Lan et al. 2016; Yang et al. 2008). However, as shown in Figure 8, the average HI mass of central galaxies is limited to a small range, $M_{\text{HI}} \sim 4 - 8 \times 10^9 M_\odot$ for halos of Milky Way masses or larger. The weak dependence on the halo mass holds even when central galaxies are divided into red and blue subsamples (see Figure 8). This result implies that, unlike the stellar content of central galaxies, which closely follows the growth of their host dark matter halos, the gas contents and gas-related evolution of central galaxies may be driven by internal and local processes. In massive halos, the central galaxies are predominantly red. Considering the large stellar mass and relatively small star formation rate as inferred by the red color, it is perhaps not surprising to see the nearly constant HI mass of these galaxies. However, the weak dependence on halo mass itself suggests that their gas-related quenching are unlikely regulated by the host halos, but rather some internal processes may be able to shut off star formation in these galaxies, making them red but do not reduce their HI gas contents significantly.

The total HI mass of galaxies as a function of dark matter halo mass, obtained using our CHIMFs and the SDSS galaxy group catalog, should be understood as the total HI mass locked in *optically-selected galaxies down to a certain limiting luminosity*. Note that the optical samples used to obtain the CLFs and to construct the group catalog have different depths. The group catalog of Yang et al. (2007) was constructed using the SDSS spectroscopic galaxy sample limited to $M_r \sim -19.5$. On the other hand, the CLFs of Lan et al. (2016) used the same group catalog to identify groups/halos, but with member galaxies identified from a much deeper photometric sample. This explains the increasing difference in the total HI mass between the prediction of the CLFs and that of the group catalog, as seen in Figure 8. The difference is larger for more massive halos where groups are observed to higher redshifts and thus may miss more satellite galaxies below the luminosity limit. To better understand this effect, we have repeated the estimation

of the HI-to-halo mass relation using different luminosity limits, from $M_r = -20.4$ down to $M_r = -14.4$. This result is shown in Figure 10, with the solid black line representing results for all galaxies, and colored lines for red/blue and central/satellite galaxies, respectively. The total HI mass based on the group catalog is plotted as solid circles with error bars in each panel, and the lower limit of HI mass predicted for the Virgo EVCC sample is plotted as pink squares with upward arrows in the last panel. For comparison, the HI mass from Guo et al. (2020) is plotted as a horizontal dotted line in each panel.

As expected, the HI mass increases as the magnitude limit goes deeper, but the increase is significant only when the luminosity limit is brighter than $M_r \sim -18$. For limits deeper than $M_r \sim -18$, the total HI mass estimated from the group catalog increases very little, while the mass estimated from the CLFs increases slowly, with a total increase of $\sim 0.1-0.2$ dex. This result is true for all types of galaxies and for halos of different masses, except for satellites in low-mass halos where the HI mass increases more rapidly with the limiting luminosity. This increase has little effect on the total HI mass, as it is dominated by central galaxies. The total HI mass from Guo et al. (2020) matches our results at a limiting luminosity that increases from $M_r \sim -17$ at $M_h \sim 10^{12} M_\odot$ to $M_r \sim -20$ at $M_h \sim 3 - 5 \times 10^{13} M_\odot$, indicating that the ALFALFA datacubes may have missed an increasingly significant fraction of HI emission from faint satellites which dominate the total HI mass in massive halos. However, it is also possible that our estimator somehow overpredicts the HI mass for satellite galaxies in massive clusters, if the gas-to-stellar mass ratio is lower for satellites in massive groups than for galaxies of similar optical properties in the general field (see subsection 5.4 for more discussion). Clearly, deeper HI surveys are needed to resolve the HI gas content in satellite galaxies of massive halos. For Virgo Cluster, our estimated HI mass (lower limits) increases with the limiting luminosity in the same way as the SDSS-based estimates, thus with a constant offset that should be attributed to the incompleteness of the EVCC galaxy catalog.

5.3. The HI-halo mass relation in theoretical studies

It is interesting to compare the HI-to-halo mass relations obtained in this paper with theoretical predictions in the literature. In Figure 8 we plot the HI-halo relation predicted by the L-GALAXIES semi-analytical model (Fu et al. 2013), by the hydrodynamical simulation Illustris (Vogelsberger et al. 2014), and by its successor IllustrisTNG (Springel et al. 2018; Marinacci et al. 2018; Naiman et al. 2018; Nelson et al. 2018; Pillepich et al.

2018). Although all the models predict a positive correlation between M_{HI} and the halo mass, they over-predict the HI mass to various degrees. In particular, at fixed halo mass the Illustris simulation predicts a total HI mass that is a factor of 3-5 higher than the observed value, while the L-Galaxies model over-predicts the HI mass for Milky Way-mass halos but a better match to the data at lower and higher halo masses. The TNG result falls in between the other two models. For central galaxies, the TNG over-predicts the HI mass at all halo masses, while Illustris over-predicts the central HI mass for low-mass halos and under-predicts it for high-mass halos. The L-Galaxies model predicts no HI gas in centrals in halos with masses above $\sim 10^{13} M_\odot$ but too much HI gas in centrals of Milky Way halos. These discrepancies must be related to the various physical recipes implemented in the simulations and the semi-analytic model to regulate gas-related processes. Our measurements of the HI-to-halo mass relation, as well as the CHIMFs, for both the total galaxy population and for different sub-populations, can provide important constraints on theoretical models.

5.4. Possible biases in the HI estimator due to environmental dependence

The fact that our model prediction for group galaxies matches observational results (see Figure 8) suggests that galaxies of similar optical properties have similar HI mass, irrespective of whether a galaxy resides in dense regions or in the general field. This result supports the basic assumption behind our HI estimator that there is a tight relation between the HI gas content and other intrinsic properties of a galaxy. However, gas stripping effects can make this relation complex. On the one hand, the HI gas may be removed without strongly affecting star formation on a timescale of < 1 Gyr (Brown et al. 2017). In this case $NUV - r$ should be better than $u - r$ for estimating the HI gas content, as the former is dominated by younger stellar populations and so can more closely trace the change in star formation. On the other hand, there are also evidences indicating that star formation can be enhanced in cluster galaxies that experience gas stripping (Roberts et al. 2021; Ramatsoku et al. 2019). This, in addition to the fact that the xGASS sample is selected for the general population of galaxies and lacks very rich groups/clusters as pointed out by Catinella et al. (2013), may lead to bias in our HI estimator, particularly for galaxies that have recently experienced gas stripping. In other words, if galaxies in rich clusters like Virgo follow different scaling relations of HI content from the average population (field galax-

ies), a bias can still be present in our HI estimator which is calibrated by galaxies mostly outside galaxy clusters.

In fact, [Zhang et al. \(2013\)](#) tested whether the HI estimator of L12 exhibits any significant biases in dense environment by examining the difference between the estimated and observed $\log(M_{\text{HI}}/M_*)$ for group/cluster galaxies as a function of the environment overdensity $\ln(1+\delta)$ (see their Figure 3). They found the L12 estimator only slightly underestimates the HI-to-stellar mass ratio by at most 0.1 dex on average, and this bias was caused by the HI-rich galaxies rather than the HI-poor galaxies in the group/clusters (thus opposite to the expectation for an environment-induced bias). Since our estimator is motivated from and quite similar to the L12 estimator, we expect our estimator to also provide unbiased HI content for galaxies in different environments. Nevertheless, considering the different calibration samples adopted in L12 and in our work, we should still keep in mind the possible bias in our estimator, especially when applying it to galaxies in dense regions. A complete and deep survey of HI 21cm emission covering a full range of environment is needed if one were to accurately quantify the possible dependence of an HI estimator on environment.

5.5. Limitations and Prospects

Our HI gas estimator is calibrated with the xGASS sample which is limited to nearby galaxies with $z < 0.05$ and $M_* > 10^9 M_\odot$. Therefore, in principle our estimator can be applied only to galaxy samples selected to these redshift and mass limits, although this estimator is shown to be able to reproduce the ALFALFA HIMF down to masses as low as $M_{\text{HI}} \sim 10^7 M_\odot$ (see [Figure 9](#)). For this reason all the results presented in this work for $M_* < 10^9 M_\odot$ should be taken in caution, and future studies with real HI observations of galaxies at lower masses would be needed to verify our predictions, e.g. the conditional HIMFs at the low-mass end.

In the near future, next generation HI surveys, such as WALLABY ([Koribalski et al. 2020](#), the Widefield ASKAP L-band Legacy All-sky Blind survey) and LADUMA ([Holwerda et al. 2012](#), Looking at the distant universe with the MeerKAT Array) will provide unprecedented HI data in the local and distant universe and improve our understanding of the HI gas content of galaxies. However, the gap between HI and optical surveys will remain for many years, and this is particularly true for low-mass and high-redshift galaxies. In the local universe, galaxies with $\log M_*/M_\odot > 9.0$ already have relatively complete HI surveys, such as xGASS and RESOLVE. Although HI surveys, such as ALFALFA, THINGS ([Walter et al. 2008](#), The H I Nearby Galaxy

Survey) and LITTLE THINGS ([Hunter et al. 2012](#), Local Irregulars That Trace Luminosity Extremes, The HI Nearby Galaxy Survey), have provided useful information about the HI gas properties for lower mass galaxies, the low-mass galaxy samples obtained are still strongly biased for HI-rich systems. For high-redshift galaxies, so far the only way to observe the HI gas content is through damped Lyman α systems. The estimator presented here, therefore, provides a way to predict and study HI gas contents for large samples of optically selected galaxies that cover large ranges of galaxy properties and redshift. For instance, [Zhang et al. \(2021\)](#) have recently attempted to estimate the HIMF of galaxies at $z \sim 1$ by applying a two-parameter HI mass estimator calibrated with nearby galaxies to the DEEP2 galaxy sample. The results obtained in the paper demonstrate that such an approach is powerful and provides an important avenue to understand cold gas contents in galaxies and in galaxy systems.

6. SUMMARY

In this paper, we introduce a new HI mass estimator in which the logarithm of the HI-to-stellar mass ratio ($\log(M_{\text{HI}}/M_*)$) is modeled by a linear combination of four galaxy properties: surface stellar mass density ($\log \mu_*$), color index ($u - r$), stellar mass ($\log M_*$) and concentration index ($\log(R_{90}/R_{50})$). The variance of individual galaxies around the mean HI mass is modeled by a Gaussian distribution. We calibrate the estimator with the xGASS sample, which is constructed to be representative for the HI content of the local galaxy population. We constrain our model parameters using Bayesian inferences and including both detections and non-detections from the xGASS sample. Applying our estimator to mock catalogs that include the same selection effects as the ALFALFA survey, we are able to statistically reproduce the distributions of both the HI mass and other galaxy properties of the real sample. We then apply our estimator to the SDSS spectroscopic galaxy sample to predict the HI mass function (HIMF) of local galaxies, as well as the conditional HI mass function (CHIMF) and the HI-halo mass relation (HIHM) for dark matter halos of different masses.

Our main results can be summarized as follows.

- The HIMF derived from the optical sample can be fitted with a single Schechter function, but with a higher amplitude and a steeper slope at HI masses below a few $\times 10^9 M_\odot$ when compared to the ALFALFA HIMF. We show that this difference is essentially caused by the cosmic variance of the local volume, which is corrected for our HIMF but not for the ALFALFA HIMF.

- We use our estimator to predict the CHIMFs for dark matter halos with $M_h \gtrsim 10^{12} M_\odot$, for both the total galaxy population and sub-populations of red/blue and central/satellite galaxies. A single Schechter function can well describe all the CHIMFs at all halo masses, except for central galaxies where a double Gaussian is preferred.
- Although red galaxies dominate the galaxy population in massive halos, red and blue galaxies have similar CHIMFs and thus contribute similarly to the total HI mass at given halo mass. This result is true for all halo masses.
- Central galaxies contribute significantly to the total HI mass only in low-mass halos, while in massive halos the majority of HI gas is associated with satellite galaxies.
- The HI mass of central galaxies shows very weak dependence on halo mass, even when divided into red and blue sub-populations. This is quite different from the total HI mass of all galaxies which increases monotonically with increasing halo mass.
- Current hydrodynamical simulations and semi-analytic models of galaxy formation fail to reproduce the HI-halo mass relation for both the central population and the total population.

ACKNOWLEDGMENTS

We are grateful to the anonymous referee for his/her comments which have helped improve our paper. XL thanks Kai Wang and Yangyao Chen for helpful discussions. This work is supported by the National Key R&D Program of China (grant No. 2018YFA0404502), and the National Natural Science Foundation of China

(grant Nos. 11821303, 11733002, 11973030, 11673015, 11733004, 11761131004, 11761141012). This work has made use of the following softwares: Numpy (Harris et al. 2020), Scipy (Virtanen et al. 2020), Matplotlib (Hunter 2007), emcee (Foreman-Mackey et al. 2013), Astropy (Astropy Collaboration et al. 2013), GetDist (Lewis 2019), seaborn (Waskom 2021), and h5py (Collette et al. 2021).

Funding for the SDSS and SDSS-II has been provided by the Alfred P. Sloan Foundation, the Participating Institutions, the National Science Foundation, the U.S. Department of Energy, the National Aeronautics and Space Administration, the Japanese Monbukagakusho, the Max Planck Society, and the Higher Education Funding Council for England. The SDSS Web Site is <http://www.sdss.org/>.

The SDSS is managed by the Astrophysical Research Consortium for the Participating Institutions. The Participating Institutions are the American Museum of Natural History, Astrophysical Institute Potsdam, University of Basel, University of Cambridge, Case Western Reserve University, University of Chicago, Drexel University, Fermilab, the Institute for Advanced Study, the Japan Participation Group, Johns Hopkins University, the Joint Institute for Nuclear Astrophysics, the Kavli Institute for Particle Astrophysics and Cosmology, the Korean Scientist Group, the Chinese Academy of Sciences (LAMOST), Los Alamos National Laboratory, the Max-Planck-Institute for Astronomy (MPIA), the Max-Planck-Institute for Astrophysics (MPA), New Mexico State University, Ohio State University, University of Pittsburgh, University of Portsmouth, Princeton University, the United States Naval Observatory, and the University of Washington.

REFERENCES

- Adams, E. A. K., Adebahr, B., de Blok, W. J. G., et al. 2022, arXiv e-prints, arXiv:2208.05348. <https://arxiv.org/abs/2208.05348>
- Adelman-McCarthy, J. K., Agüeros, M. A., Allam, S. S., et al. 2008, *The Astrophysical Journal Supplement Series*, 175, 297, doi: [10.1086/524984](https://doi.org/10.1086/524984)
- Astropy Collaboration, Robitaille, T. P., Tollerud, E. J., et al. 2013, *A&A*, 558, A33, doi: [10.1051/0004-6361/201322068](https://doi.org/10.1051/0004-6361/201322068)
- Baldry, I. K., Glazebrook, K., Brinkmann, J., et al. 2004, *ApJ*, 600, 681, doi: [10.1086/380092](https://doi.org/10.1086/380092)
- Barnes, L. A., & Haehnelt, M. G. 2014, *MNRAS*, 440, 2313, doi: [10.1093/mnras/stu445](https://doi.org/10.1093/mnras/stu445)
- Blanton, M. R., Kazin, E., Muna, D., Weaver, B. A., & Price-Whelan, A. 2011, *AJ*, 142, 31, doi: [10.1088/0004-6256/142/1/31](https://doi.org/10.1088/0004-6256/142/1/31)
- Blanton, M. R., Lupton, R. H., Schlegel, D. J., et al. 2005, *ApJ*, 631, 208, doi: [10.1086/431416](https://doi.org/10.1086/431416)
- Blanton, M. R., & Moustakas, J. 2009, *ARA&A*, 47, 159, doi: [10.1146/annurev-astro-082708-101734](https://doi.org/10.1146/annurev-astro-082708-101734)
- Blanton, M. R., & Roweis, S. 2007, *AJ*, 133, 734, doi: [10.1086/510127](https://doi.org/10.1086/510127)
- Blanton, M. R., Schlegel, D. J., Strauss, M. A., et al. 2005, *The Astronomical Journal*, 129, 2562, doi: [10.1086/429803](https://doi.org/10.1086/429803)

- Bloom, J. V., Croom, S. M., Bryant, J. J., et al. 2017, *Monthly Notices of the Royal Astronomical Society*, 472, 1809, doi: [10.1093/mnras/stx1701](https://doi.org/10.1093/mnras/stx1701)
- Boselli, A., & Gavazzi, G. 2006, *PASP*, 118, 517, doi: [10.1086/500691](https://doi.org/10.1086/500691)
- Brown, T., Catinella, B., Cortese, L., et al. 2015, *MNRAS*, 452, 2479, doi: [10.1093/mnras/stv1311](https://doi.org/10.1093/mnras/stv1311)
- . 2017, *MNRAS*, 466, 1275, doi: [10.1093/mnras/stw2991](https://doi.org/10.1093/mnras/stw2991)
- Bruzual, G., & Charlot, S. 2003, *MNRAS*, 344, 1000, doi: [10.1046/j.1365-8711.2003.06897.x](https://doi.org/10.1046/j.1365-8711.2003.06897.x)
- Calette, A. R., Avila-Reese, V., Rodríguez-Puebla, A., Lagos, C. d. P., & Catinella, B. 2021a, *MNRAS*, 505, 304, doi: [10.1093/mnras/stab1282](https://doi.org/10.1093/mnras/stab1282)
- Calette, A. R., Rodríguez-Puebla, A., Avila-Reese, V., & Lagos, C. d. P. 2021b, *MNRAS*, 506, 1507, doi: [10.1093/mnras/stab1788](https://doi.org/10.1093/mnras/stab1788)
- Catinella, B., Schiminovich, D., Kauffmann, G., et al. 2010, *MNRAS*, 403, 683, doi: [10.1111/j.1365-2966.2009.16180.x](https://doi.org/10.1111/j.1365-2966.2009.16180.x)
- Catinella, B., Schiminovich, D., Cortese, L., et al. 2013, *MNRAS*, 436, 34, doi: [10.1093/mnras/stt1417](https://doi.org/10.1093/mnras/stt1417)
- Catinella, B., Saintonge, A., Janowiecki, S., et al. 2018, *Monthly Notices of the Royal Astronomical Society*, 476, 875, doi: [10.1093/mnras/sty089](https://doi.org/10.1093/mnras/sty089)
- Chabrier, G. 2003, *PASP*, 115, 763, doi: [10.1086/376392](https://doi.org/10.1086/376392)
- Chauhan, G., Lagos, C. d. P., Stevens, A. R. H., et al. 2021, *MNRAS*, 506, 4893, doi: [10.1093/mnras/stab1925](https://doi.org/10.1093/mnras/stab1925)
- . 2020, *MNRAS*, 498, 44, doi: [10.1093/mnras/staa2251](https://doi.org/10.1093/mnras/staa2251)
- Chemin, L., Carignan, C., & Foster, T. 2009, *ApJ*, 705, 1395, doi: [10.1088/0004-637X/705/2/1395](https://doi.org/10.1088/0004-637X/705/2/1395)
- Chen, Y., Mo, H. J., Li, C., et al. 2019, *ApJ*, 872, 180, doi: [10.3847/1538-4357/ab0208](https://doi.org/10.3847/1538-4357/ab0208)
- Collette, A., Kluyver, T., Caswell, T. A., et al. 2021, *h5py/h5py: 3.5.0, 3.5.0*, Zenodo, Zenodo, doi: [10.5281/zenodo.5585380](https://doi.org/10.5281/zenodo.5585380)
- Cowie, L. L., & Songaila, A. 1977, *Nature*, 266, 501, doi: [10.1038/266501a0](https://doi.org/10.1038/266501a0)
- Davé, R., Crain, R. A., Stevens, A. R. H., et al. 2020, *MNRAS*, 497, 146, doi: [10.1093/mnras/staa1894](https://doi.org/10.1093/mnras/staa1894)
- Driver, S. P., Hill, D. T., Kelvin, L. S., et al. 2011, *MNRAS*, 413, 971, doi: [10.1111/j.1365-2966.2010.18188.x](https://doi.org/10.1111/j.1365-2966.2010.18188.x)
- Driver, S. P., Robotham, A. S. G., Obreschkow, D., et al. 2022, *MNRAS*, 515, 2138, doi: [10.1093/mnras/stac581](https://doi.org/10.1093/mnras/stac581)
- Eckert, K. D., Kannappan, S. J., Stark, D. V., et al. 2015, *ApJ*, 810, 166, doi: [10.1088/0004-637X/810/2/166](https://doi.org/10.1088/0004-637X/810/2/166)
- Foreman-Mackey, D., Hogg, D. W., Lang, D., & Goodman, J. 2013, *PASP*, 125, 306, doi: [10.1086/670067](https://doi.org/10.1086/670067)
- Freeland, E., Stilp, A., & Wilcots, E. 2009, *AJ*, 138, 295, doi: [10.1088/0004-6256/138/1/295](https://doi.org/10.1088/0004-6256/138/1/295)
- Fu, J., Kauffmann, G., Huang, M.-l., et al. 2013, *MNRAS*, 434, 1531, doi: [10.1093/mnras/stt1117](https://doi.org/10.1093/mnras/stt1117)
- Giovanelli, R., Haynes, M. P., Kent, B. R., et al. 2005, *The Astronomical Journal*, 130, 2598, doi: [10.1086/497431](https://doi.org/10.1086/497431)
- Gunn, J. E., & Gott, J. Richard, I. 1972, *ApJ*, 176, 1, doi: [10.1086/151605](https://doi.org/10.1086/151605)
- Guo, H., Jones, M. G., Haynes, M. P., & Fu, J. 2020, *ApJ*, 894, 92, doi: [10.3847/1538-4357/ab886f](https://doi.org/10.3847/1538-4357/ab886f)
- Guo, H., Li, C., Zheng, Z., et al. 2017, *ApJ*, 846, 61, doi: [10.3847/1538-4357/aa85e7](https://doi.org/10.3847/1538-4357/aa85e7)
- Harris, C. R., Millman, K. J., van der Walt, S. J., et al. 2020, *Nature*, 585, 357, doi: [10.1038/s41586-020-2649-2](https://doi.org/10.1038/s41586-020-2649-2)
- Haynes, M. P., & Giovanelli, R. 1984, *AJ*, 89, 758, doi: [10.1086/113573](https://doi.org/10.1086/113573)
- Haynes, M. P., Giovanelli, R., Martin, A. M., et al. 2011, *The Astronomical Journal*, 142, 170, doi: [10.1088/0004-6256/142/5/170](https://doi.org/10.1088/0004-6256/142/5/170)
- Haynes, M. P., Giovanelli, R., Kent, B. R., et al. 2018, *ApJ*, 861, 49, doi: [10.3847/1538-4357/aac956](https://doi.org/10.3847/1538-4357/aac956)
- Hess, K. M., & Wilcots, E. M. 2013, *AJ*, 146, 124, doi: [10.1088/0004-6256/146/5/124](https://doi.org/10.1088/0004-6256/146/5/124)
- Holwerda, B. W., Blyth, S. L., & Baker, A. J. 2012, in *The Spectral Energy Distribution of Galaxies - SED 2011*, ed. R. J. Tuffs & C. C. Popescu, Vol. 284, 496–499, doi: [10.1017/S1743921312009702](https://doi.org/10.1017/S1743921312009702)
- Hunter, D. A., Ficut-Vicas, D., Ashley, T., et al. 2012, *AJ*, 144, 134, doi: [10.1088/0004-6256/144/5/134](https://doi.org/10.1088/0004-6256/144/5/134)
- Hunter, J. D. 2007, *Computing in Science and Engineering*, 9, 90, doi: [10.1109/MCSE.2007.55](https://doi.org/10.1109/MCSE.2007.55)
- Jones, M. G., Haynes, M. P., Giovanelli, R., & Moorman, C. 2018a, *MNRAS*, 477, 2, doi: [10.1093/mnras/sty521](https://doi.org/10.1093/mnras/sty521)
- Jones, M. G., Hess, K. M., Adams, E. A. K., & Verdes-Montenegro, L. 2020, *MNRAS*, 494, 2090, doi: [10.1093/mnras/staa810](https://doi.org/10.1093/mnras/staa810)
- Jones, M. G., Papastergis, E., Haynes, M. P., & Giovanelli, R. 2016, *MNRAS*, 457, 4393, doi: [10.1093/mnras/stw263](https://doi.org/10.1093/mnras/stw263)
- Jones, M. G., Espada, D., Verdes-Montenegro, L., et al. 2018b, *A&A*, 609, A17, doi: [10.1051/0004-6361/201731448](https://doi.org/10.1051/0004-6361/201731448)
- Kalberla, P. M. W., & Kerp, J. 2009, *ARA&A*, 47, 27, doi: [10.1146/annurev-astro-082708-101823](https://doi.org/10.1146/annurev-astro-082708-101823)
- Kannappan, S. J. 2004, *ApJL*, 611, L89, doi: [10.1086/423785](https://doi.org/10.1086/423785)
- Kennicutt, Robert C., J. 1998, *ApJ*, 498, 541, doi: [10.1086/305588](https://doi.org/10.1086/305588)
- Kewley, L. J., Dopita, M. A., Sutherland, R. S., Heisler, C. A., & Trevena, J. 2001, *ApJ*, 556, 121, doi: [10.1086/321545](https://doi.org/10.1086/321545)
- Kilborn, V. A., Forbes, D. A., Barnes, D. G., et al. 2009, *MNRAS*, 400, 1962, doi: [10.1111/j.1365-2966.2009.15587.x](https://doi.org/10.1111/j.1365-2966.2009.15587.x)

- Kim, S., Rey, S.-C., Jerjen, H., et al. 2014, *ApJS*, 215, 22, doi: [10.1088/0067-0049/215/2/22](https://doi.org/10.1088/0067-0049/215/2/22)
- Koribalski, B. S., Staveley-Smith, L., Westmeier, T., et al. 2020, *Ap&SS*, 365, 118, doi: [10.1007/s10509-020-03831-4](https://doi.org/10.1007/s10509-020-03831-4)
- Lan, T.-W., Ménard, B., & Mo, H. 2016, *MNRAS*, 459, 3998, doi: [10.1093/mnras/stw898](https://doi.org/10.1093/mnras/stw898)
- Lewis, A. 2019, arXiv e-prints, arXiv:1910.13970. <https://arxiv.org/abs/1910.13970>
- Li, C., Kauffmann, G., Fu, J., et al. 2012, *MNRAS*, 424, 1471, doi: [10.1111/j.1365-2966.2012.21337.x](https://doi.org/10.1111/j.1365-2966.2012.21337.x)
- Li, C., Kauffmann, G., Jing, Y. P., et al. 2006, *MNRAS*, 368, 21, doi: [10.1111/j.1365-2966.2006.10066.x](https://doi.org/10.1111/j.1365-2966.2006.10066.x)
- Li, C., & White, S. D. M. 2009, *MNRAS*, 398, 2177, doi: [10.1111/j.1365-2966.2009.15268.x](https://doi.org/10.1111/j.1365-2966.2009.15268.x)
- Li, Z., Guo, H., & Mao, Y. 2022, arXiv e-prints, arXiv:2207.10414. <https://arxiv.org/abs/2207.10414>
- Lim, S. H., Mo, H. J., Lu, Y., Wang, H., & Yang, X. 2017, *MNRAS*, 470, 2982, doi: [10.1093/mnras/stx1462](https://doi.org/10.1093/mnras/stx1462)
- Loveday, J., Norberg, P., Baldry, I. K., et al. 2015, *MNRAS*, 451, 1540, doi: [10.1093/mnras/stv1013](https://doi.org/10.1093/mnras/stv1013)
- Lu, Y., Yang, X., Liu, C., et al. 2020, arXiv e-prints, arXiv:2008.09804. <https://arxiv.org/abs/2008.09804>
- Marinacci, F., Vogelsberger, M., Pakmor, R., et al. 2018, *MNRAS*, 480, 5113, doi: [10.1093/mnras/sty2206](https://doi.org/10.1093/mnras/sty2206)
- Martin, A. M., Giovanelli, R., Haynes, M. P., & Guzzo, L. 2012, *ApJ*, 750, 38, doi: [10.1088/0004-637X/750/1/38](https://doi.org/10.1088/0004-637X/750/1/38)
- Martin, D. C., Fanson, J., Schiminovich, D., et al. 2005, *The Astrophysical Journal*, 619, L1, doi: [10.1086/426387](https://doi.org/10.1086/426387)
- Meyer, M. J., Zwaan, M. A., Webster, R. L., et al. 2004, *MNRAS*, 350, 1195, doi: [10.1111/j.1365-2966.2004.07710.x](https://doi.org/10.1111/j.1365-2966.2004.07710.x)
- Mo, H., van den Bosch, F. C., & White, S. 2010, *Galaxy Formation and Evolution*
- Moorman, C. M., Vogeley, M. S., Hoyle, F., et al. 2014, *MNRAS*, 444, 3559, doi: [10.1093/mnras/stu1674](https://doi.org/10.1093/mnras/stu1674)
- Naiman, J. P., Pillepich, A., Springel, V., et al. 2018, *MNRAS*, 477, 1206, doi: [10.1093/mnras/sty618](https://doi.org/10.1093/mnras/sty618)
- Nelson, D., Pillepich, A., Springel, V., et al. 2018, *MNRAS*, 475, 624, doi: [10.1093/mnras/stx3040](https://doi.org/10.1093/mnras/stx3040)
- Nulsen, P. E. J. 1982, *MNRAS*, 198, 1007, doi: [10.1093/mnras/198.4.1007](https://doi.org/10.1093/mnras/198.4.1007)
- Obuljen, A., Alonso, D., Villaescusa-Navarro, F., Yoon, I., & Jones, M. 2019, *MNRAS*, 486, 5124, doi: [10.1093/mnras/stz1118](https://doi.org/10.1093/mnras/stz1118)
- Papastergis, E., Giovanelli, R., Haynes, M. P., Rodríguez-Puebla, A., & Jones, M. G. 2013, *ApJ*, 776, 43, doi: [10.1088/0004-637X/776/1/43](https://doi.org/10.1088/0004-637X/776/1/43)
- Paul, N., Choudhury, T. R., & Paranjape, A. 2018, *MNRAS*, 479, 1627, doi: [10.1093/mnras/sty1539](https://doi.org/10.1093/mnras/sty1539)
- Pillepich, A., Nelson, D., Hernquist, L., et al. 2018, *MNRAS*, 475, 648, doi: [10.1093/mnras/stx3112](https://doi.org/10.1093/mnras/stx3112)
- Pisano, D. J., Barnes, D. G., Staveley-Smith, L., et al. 2011, *ApJS*, 197, 28, doi: [10.1088/0067-0049/197/2/28](https://doi.org/10.1088/0067-0049/197/2/28)
- Praton, E. A., & Schneider, S. E. 1994, *ApJ*, 422, 46, doi: [10.1086/173702](https://doi.org/10.1086/173702)
- Rafieferantsoa, M., Andrianomena, S., & Davé, R. 2018, *MNRAS*, 479, 4509, doi: [10.1093/mnras/sty1777](https://doi.org/10.1093/mnras/sty1777)
- Ramatsoku, M., Serra, P., Poggianti, B. M., et al. 2019, *MNRAS*, 487, 4580, doi: [10.1093/mnras/stz1609](https://doi.org/10.1093/mnras/stz1609)
- Roberts, I. D., van Weeren, R. J., McGee, S. L., et al. 2021, *A&A*, 652, A153, doi: [10.1051/0004-6361/202141118](https://doi.org/10.1051/0004-6361/202141118)
- Schechter, P. 1976, *ApJ*, 203, 297, doi: [10.1086/154079](https://doi.org/10.1086/154079)
- Schmidt, M. 1963, *ApJ*, 137, 758, doi: [10.1086/147553](https://doi.org/10.1086/147553)
- Springel, V., Pakmor, R., Pillepich, A., et al. 2018, *MNRAS*, 475, 676, doi: [10.1093/mnras/stx3304](https://doi.org/10.1093/mnras/stx3304)
- Stevens, A. R. H., Diemer, B., Lagos, C. d. P., et al. 2019, *MNRAS*, 483, 5334, doi: [10.1093/mnras/sty3451](https://doi.org/10.1093/mnras/sty3451)
- Stierwalt, S., Haynes, M. P., Giovanelli, R., et al. 2009, *AJ*, 138, 338, doi: [10.1088/0004-6256/138/2/338](https://doi.org/10.1088/0004-6256/138/2/338)
- Teimoorinia, H., Ellison, S. L., & Patton, D. R. 2017, *MNRAS*, 464, 3796, doi: [10.1093/mnras/stw2606](https://doi.org/10.1093/mnras/stw2606)
- Toribio, M. C., Solanes, J. M., Giovanelli, R., Haynes, M. P., & Masters, K. L. 2011, *ApJ*, 732, 92, doi: [10.1088/0004-637X/732/2/92](https://doi.org/10.1088/0004-637X/732/2/92)
- Tremonti, C. A., Heckman, T. M., Kauffmann, G., et al. 2004, *ApJ*, 613, 898, doi: [10.1086/423264](https://doi.org/10.1086/423264)
- Villaescusa-Navarro, F., Genel, S., Castorina, E., et al. 2018, *ApJ*, 866, 135, doi: [10.3847/1538-4357/aadba0](https://doi.org/10.3847/1538-4357/aadba0)
- Virtanen, P., Gommers, R., Oliphant, T. E., et al. 2020, *Nature Methods*, 17, 261, doi: [10.1038/s41592-019-0686-2](https://doi.org/10.1038/s41592-019-0686-2)
- Vogelsberger, M., Genel, S., Springel, V., et al. 2014, *MNRAS*, 444, 1518, doi: [10.1093/mnras/stu1536](https://doi.org/10.1093/mnras/stu1536)
- Walter, F., Brinks, E., de Blok, W. J. G., et al. 2008, *AJ*, 136, 2563, doi: [10.1088/0004-6256/136/6/2563](https://doi.org/10.1088/0004-6256/136/6/2563)
- Wang, H., Mo, H. J., Yang, X., Jing, Y. P., & Lin, W. P. 2014, *ApJ*, 794, 94, doi: [10.1088/0004-637X/794/1/94](https://doi.org/10.1088/0004-637X/794/1/94)
- Wang, J., Staveley-Smith, L., Westmeier, T., et al. 2021, *ApJ*, 915, 70, doi: [10.3847/1538-4357/abfc52](https://doi.org/10.3847/1538-4357/abfc52)
- Wang, S., Wang, J., For, B.-Q., et al. 2022, *ApJ*, 927, 66, doi: [10.3847/1538-4357/ac4270](https://doi.org/10.3847/1538-4357/ac4270)
- Waskom, M. L. 2021, *Journal of Open Source Software*, 6, 3021, doi: [10.21105/joss.03021](https://doi.org/10.21105/joss.03021)
- Wechsler, R. H., & Tinker, J. L. 2018, *ARA&A*, 56, 435, doi: [10.1146/annurev-astro-081817-051756](https://doi.org/10.1146/annurev-astro-081817-051756)
- Westmeier, T., Obreschkow, D., Calabretta, M., et al. 2017, *MNRAS*, 472, 4832, doi: [10.1093/mnras/stx2289](https://doi.org/10.1093/mnras/stx2289)
- White, S. D. M., & Rees, M. J. 1978, *MNRAS*, 183, 341, doi: [10.1093/mnras/183.3.341](https://doi.org/10.1093/mnras/183.3.341)

- Wong, O. I., Ryan-Weber, E. V., Garcia-Appadoo, D. A., et al. 2006, MNRAS, 371, 1855, doi: [10.1111/j.1365-2966.2006.10846.x](https://doi.org/10.1111/j.1365-2966.2006.10846.x)
- Yang, X., Mo, H. J., & van den Bosch, F. C. 2008, ApJ, 676, 248, doi: [10.1086/528954](https://doi.org/10.1086/528954)
- . 2009, ApJ, 695, 900, doi: [10.1088/0004-637X/695/2/900](https://doi.org/10.1088/0004-637X/695/2/900)
- Yang, X., Mo, H. J., van den Bosch, F. C., et al. 2007, ApJ, 671, 153, doi: [10.1086/522027](https://doi.org/10.1086/522027)
- York, D. G., Adelman, J., Anderson, John E., J., et al. 2000, AJ, 120, 1579, doi: [10.1086/301513](https://doi.org/10.1086/301513)
- Zhang, W., Kauffmann, G., Wang, J., et al. 2021, A&A, 648, A25, doi: [10.1051/0004-6361/202039878](https://doi.org/10.1051/0004-6361/202039878)
- Zhang, W., Li, C., Kauffmann, G., & Xiao, T. 2013, MNRAS, 429, 2191, doi: [10.1093/mnras/sts490](https://doi.org/10.1093/mnras/sts490)
- Zhang, W., Li, C., Kauffmann, G., et al. 2009, MNRAS, 397, 1243, doi: [10.1111/j.1365-2966.2009.15050.x](https://doi.org/10.1111/j.1365-2966.2009.15050.x)
- Zu, Y. 2020, MNRAS, 496, 111, doi: [10.1093/mnras/staa1457](https://doi.org/10.1093/mnras/staa1457)
- Zwaan, M. A., Meyer, M. J., Staveley-Smith, L., & Webster, R. L. 2005, MNRAS, 359, L30, doi: [10.1111/j.1745-3933.2005.00029.x](https://doi.org/10.1111/j.1745-3933.2005.00029.x)